Incorporating Solar Activity into General Perturbations Analysis of Atmospheric Friction

Emma Kerr* and Malcolm Macdonald†
University of Strathclyde, Glasgow, Scotland, G1 1XJ

A new parameter is introduced, termed the density index, which enables the solar activity cycle to be captured in a new analytical atmospheric density model. Consequentially, a new solar activity model is developed that uses a single independent variable per solar cycle to describe the solar activity across that cycle, as indicated by the $F_{10.7}$ index. These models are combined and applied to a well-known general perturbations method for satellite orbit lifetime analysis, which is first modified using modern mathematical tools to remove simplifications in the derivation. Validation against historical data shows an improvement in orbit lifetime estimates from an average error of 50.44 percent with a standard deviation of 24.96 percent, to an average error of 3.46 percent with a standard deviation of 3.25 percent. Furthermore, the new method with applied atmospheric and solar activity models is found to compare favorably against other general and special perturbations methods, including third party, and commercial software, the most accurate of which was found to have an average error of 6.63 percent and standard deviation of 7.00 percent. A case study, the UKube-1 spacecraft, is presented and it is found that the spacecraft was inserted into an orbit 54km lower than required to comply with best-practice guidelines, and that with 1σ confidence its orbit will decay in June 2028 ± 2 years, and June 2028 ± 4 months if the next solar cycle is an average magnitude cycle.

---

* PhD Candidate, Mechanical and Aerospace Engineering, University of Strathclyde, Glasgow, G1 1XJ, AIAA Student Member.
† Reader, Mechanical and Aerospace Engineering, University of Strathclyde, Glasgow, G1 1XJ, AIAA Associate Fellow.

I. Introduction

INCREASING concern over littering of the space environment with so-called space debris is driving efforts towards improved orbit lifetime estimation approaches, and towards improved regulations on the behavior of spacecraft launched into particular regions of the near-Earth environment. Among the most prominent of relevant documents are the Inter-Agency space Debris coordination Committee (IADC) "Space Debris Mitigation Guidelines", and the International Organization for Standardization (ISO) "Space systems - Space debris mitigation requirements" [1,2]. Both of these documents state that a spacecraft should be removed within 25 years of decommissioning if it travels through either of the protected regions detailed in the guidelines: Low Earth Orbit (LEO) and Geostationary Earth Orbit (GEO). As these guidelines specify a time period in which spacecraft should be removed, a further standard has been generated by ISO discussing the estimation of orbit lifetime [3]. This standard and the work done to generate it, particularly the work by Oltrogge and Chao [4], discuss the advantages and disadvantages of three different methods for orbit lifetime estimation and give guidance on how to use each method effectively. The methods detailed are, high precision numerical integration, rapid semi-analytical orbit propagation, and numerical table look-up analysis and fit formula evaluations. There is however one further method not considered, general perturbations methods, often termed as analytical methods. This method is often dismissed for long-term orbit propagation due to problems with accuracy [5]; this paper addresses and resolves this challenge.

Primary body atmospheric friction (commonly referred to as 'atmospheric drag') acts against the velocity vector resulting in a reduction in orbit energy, and hence semi-major axis. Consequently, it is the principal contributor to artificial satellite orbit decay in Earth orbit below 1000 km altitude. The magnitude of this frictional force is directly proportional to the atmospheric density, which is intrinsically time-variant due the influence of solar activity, leading to significant variations in the atmospheric density over time at even the same altitude [6]. Naasz, Berry, and Schatten use propriety third-party software, applying special perturbations methods, to show the impact of variations in solar activity on satellite orbital lifetime predictions [7], confirming the correlation between high solar activity levels and shorter orbit lifetimes, and conversely low solar activity levels and longer orbit lifetimes. Vallado and Finkleman extend that work to consider the effect of solar cycle variations on orbit lifetime predictions, once again applying special perturbations methods to find a direct relationship between solar activity and orbit lifetime [8]. More specifically, they found that solar activity was the largest contributor to variation in atmospheric density at a fixed altitude. Consequently, the effect of solar activity cannot be neglected. However, general

perturbations methods taking into consideration atmospheric drag commonly neglect solar activity, leading to a significant lack of accuracy in such methods.

Vallado and Finkleman also discuss the solar radio flux at wavelength 10.7 cm (2800 MHz), the $F_{10.7}$ index, which is commonly used as an indicator of the solar activity level, and its use in empirical models of atmospheric density, finding that it is the most suitable proxy for solar activity [8]. The $F_{10.7}$ index is used herein as the measure of solar activity.

The most commonly cited general perturbations method for predicting the orbital lifetime of low-eccentricity satellites in the presence of a time-invariant and a spherically symmetrical retarding atmosphere is the method presented by Cook, King-Hele and Walker, but later expanded by King-Hele. Herein referred to as the King-Hele method [9,10]. This method is based on power series expansions of the eccentricity, semi-major axis, and eccentric anomaly. It is also worth mentioning that there are many other methods of orbit lifetime prediction such as that presented by Swinerd and Boulton, who adopt Cook, King-Hele and Walker's power expansion method and produce orbital lifetime equations incorporating the effect of atmospheric oblateness with diurnal density variations [11]. Griffin and French also built on the work of Cook, King-Hele and Walker, introducing a new equation for the orbit lifetime of spacecraft in initially circular orbits [12]. In a series of papers Sharma takes a different approach, using K-S elements to build the analytical solution for orbit lifetime prediction [13–16]. Sharma first explores a basic method with test cases covering the eccentricity range from 0.001 to 0.1. The method is then improved by expanding to include higher order terms with test cases with eccentricities in the range 0.001 to 0.8. Martinusi, Dell'Elce and Kerschen have demonstrated an averaging technique used to obtain a first-order approximate solution for the motion of a satellite in low Earth orbit [17,18]. However, no author has published so extensively, and with such a thorough approach, as King-Hele and his various co-authors, who over the years have systematically presented papers detailing the impact of various effects on the orbit decay of satellites in Earth orbit. An 8-part series of papers titled "The Contraction of Satellite Orbits Under the Influence of Air Drag" explores various effects and the corresponding orbit lifetime prediction methods dealing with these effects. Part 1 in the series introduces a basic method for orbit lifetime prediction of satellites in low eccentricity ($e<0.2$) orbits, which is then expanded in part 2 to address the issue of an oblate atmosphere [9,19]. Part 3 addresses higher eccentricity orbits ($0.2 \leq e < 1$) [20]. Part 4 builds on part 1 to include the effect of variations in scale height with altitude [21]. Then part 5 builds on part 2 to include the day-to-night variation in atmospheric density [22]. Part 6 builds on part 5 looking in more depth at the

effects of day-to-night variation in density on near-circular orbits [23]. Part 7 combines work from parts 3 and 5 by examining the effects of altitude varying scale height on high eccentricity orbits [24]. Finally, part 8 looks at how perturbations due to odd zonal harmonics of the geopotential affect the orbit lifetime of a satellite in an oblate atmosphere [25]. It is noteworthy that despite this detailed and methodical approach that the effect of solar activity was not addressed in this series of papers. Another important point of interest is that in many cases general perturbations methods are not validated. Where validation is considered, typically the methods are compared with numerical methods to ascertain their accuracy. There is, in this comparison, an inherent presumption that the numerical method is accurate, however numerical methods are still approximations, though to a lesser degree than analytical models, and are therefore subject to error when compared to real cases. Therefore, in this work validation is done using historical data from real missions, removing the uncertainty attached to a numerical method comparison.

At this stage it is worth noting the promising results from Barrio and Palacián [26]; they propose a method for orbit lifetime analysis of high eccentricity orbits based on Lie transformations. The results suggest their theory may be useful in simulating geosynchronous transfer orbits, whilst herein an initial application focus is placed on low eccentricity orbits, though the methods developed can be applied to any orbit model. The work of Titov, Burt and Josyula is also of interest as they demonstrate the importance of understanding the accuracy of input parameters and their uncertainties [27]. They particularly focus on quantifying uncertainties in the computed flow parameters from a hypersonic aerothermodynamic particle implementation of a direct simulation Monte Carlo solution for spacecraft drag. They show that uncertainties in the atmospheric density input parameter are the main contributor to uncertainty in the drag force; however, no consideration was given to separating the solar activity as a source of uncertainty. They also discuss propagating the input parameter uncertainties through the model to produce an estimate of the contribution to the resulting output uncertainty.

To the best of the author's knowledge, the only attempt made to consider the effect of solar activity in general perturbations methods was made by King-Hele and Walker [28]. They incorporate the solar activity using a so-called 'solar cycle factor', which is a basic correction factor applied to the orbit lifetime estimate after the prediction (neglecting solar activity) has been made. While this method could be employed for back-of-an-envelope calculations, it does not capture the mechanism by which solar activity affects the spacecraft drag calculation, and as such it would be unlikely to give reliable results.

To incorporate solar activity induced variations on atmospheric density the stochastic nature of solar activity must be considered. When this is introduced to the atmospheric density calculation, which in turn is applied to the orbit calculation, the solution becomes time dependent due to the variability in solar activity, within the current cycle and from cycle to cycle. Therefore the mission epoch must be considered.

Modelling the solar activity cycle accurately is critical to gaining an accurate model atmospheric density. Considerable attention has been given to predicting variations in the solar activity cycle. For example, Schatten has published extensively in collaboration with various authors on the solar activity cycle and solar activity [29–32]. To study the solar activity cycle in general terms, many authors have focused specifically on the shape of the cycle and its apparent deviation from a typical periodic sinusoid [33–35]. A similar approach is developed herein.

A new parameter, the 'density index', is introduced to incorporate the effect of solar activity in the calculation of the atmospheric density used in orbit predictions. The King-Hele method is modified using modern mathematical tools to remove some of the simplifications in the derivation of the orbital lifetime equations. The Modified King-Hele method is applied, with the new solar activity and atmospheric density models, to a set of historical missions in order to validate the method. Furthermore, an accuracy comparison of the Modified King-Hele method to other orbit lifetime estimation methods is drawn. The method is also applied within a Monte Carlo analysis to give a confidence interval as well as an orbit lifetime estimation. Finally, the method is applied to a case study of the UKube-1 spacecraft (COSPAR spacecraft identification 2014-037F) to demonstrate its use on non-historical spacecraft [10]. It should be noted, notwithstanding the application focus herein to long-duration trajectory propagation using the Modified King-Hele method for low eccentricity orbits that the methods developed herein can be applied to any orbit general perturbations or semi-analytical/semi-numerical model.

II. Atmospheric Density Model

Calculating atmospheric density at a given altitude is, as previously noted, challenging due to the time-variant nature of the atmosphere and the complexity of the interactions affecting it. Atmospheric models can be static profiles, global analytical fits, or time-variant [6]. Time-variant models aim to capture causes of temperature fluctuations in the upper atmosphere. For example, extreme ultraviolet radiation from the Sun causes near-instantaneous heating of the upper atmosphere, and hence rapidly effects atmospheric density [6]. Meanwhile, other

causes of atmospheric heating, such as geomagnetic activity, exhibit a cause and effect delay making their effects much more difficult to capture [6].

Using total atmospheric density data from the Committee on Space Research International Reference Atmosphere [36], commonly known as CIRA or CIRA-12, an analytical equation for the Earth's atmospheric density is derived using regression analysis, as will be detailed later. The CIRA model was chosen as it incorporates many of the most notable atmosphere models in current literature; including, but not limited to, NRLMSISE-00 [37], JB2008 [38,39], GRAM-07 [40], and DTM [41]. As will be discussed later, the new density index parameter is then applied to capture solar activity effects. The approach taken to develop a global analytical fit for the Earth's atmospheric density negates the need for input parameters such as the local apparent solar time, or geodetic latitude and longitude, which are both typically required by empirical and time-variant models. However, it does potentially limit the methods applicability to, for example, non-Sun-synchronous orbits where the fixed local apparent solar time, and hence the atmospheric diurnal effects, may not be well-captured.

Regression analysis, specifically curve fitting, is used to fit an equation to the CIRA data. Traditionally, an exponential curve fit is used, however such curves are generally only applicable when considering altitudes up to 100km; when considering higher altitudes they become less accurate [5]. Macdonald et al. proposed a power fit model however did not expand on how accurate it may be in comparison to the exponential fit [42].

The exponential model connects the altitude to atmospheric density as

$$\rho = \rho_r e^{\frac{h_r - h}{H}} \tag{1}$$

where ρ is the atmospheric density, ρ_r is the atmospheric density at a reference altitude, h is the altitude, h_r is the reference altitude and H is the density scale height. For elliptical orbits the altitudes are typically taken at periapsis. The difficulty in using this formulation is that it hinges on the use of a reference density and scale height, which are arbitrarily chosen. An expert in atmospheric modelling could arguably use this formulation effectively; however a layman would be unlikely to. The power model connects the altitude to the atmospheric density as

$$\rho = Ah^B \tag{2}$$

where A and B are independent variables derived in the curve fitting.

The exponential model, being the traditional approach, is more often discussed but as can be seen in Fig. 1 the power model provides a visibly more accurate fit. The coefficients of determination, R^2, of each of the two curves are shown in Fig. 1, verifying mathematically that the power curve is the better fit.

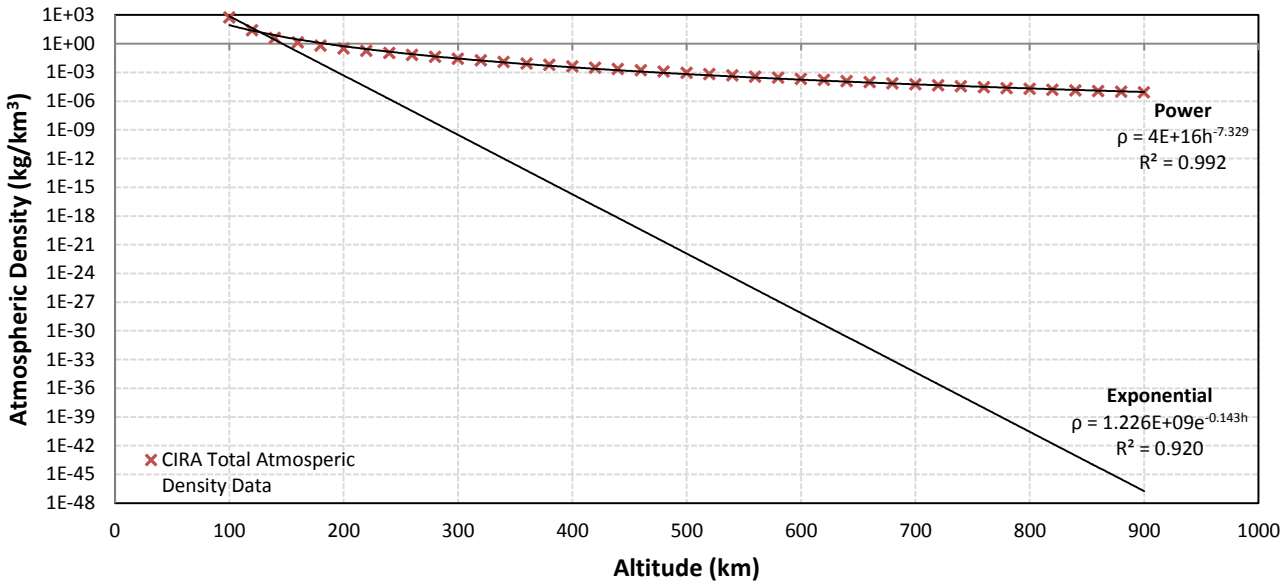

Fig. 1 Power and exponential curve-fit model comparison for average total atmospheric density; with CIRA-12 data also shown as crosses (N.B. logarithmic y-axis).

The curves shown in Fig. 1 model the average total atmospheric density data. However, the CIRA model provides data for low, average, and high solar activity conditions, corresponding to values of 70, 140, and 250 Solar Flux Units, SFU, respectively [36]. This data is therefore used to generate two further power curves, see Fig. 2, to describe the total atmospheric density with relation to altitude and solar activity level. The coefficients required to reproduce the curve fits shown in Fig. 2, using Eq. (2), can be found in the appendix to this paper.

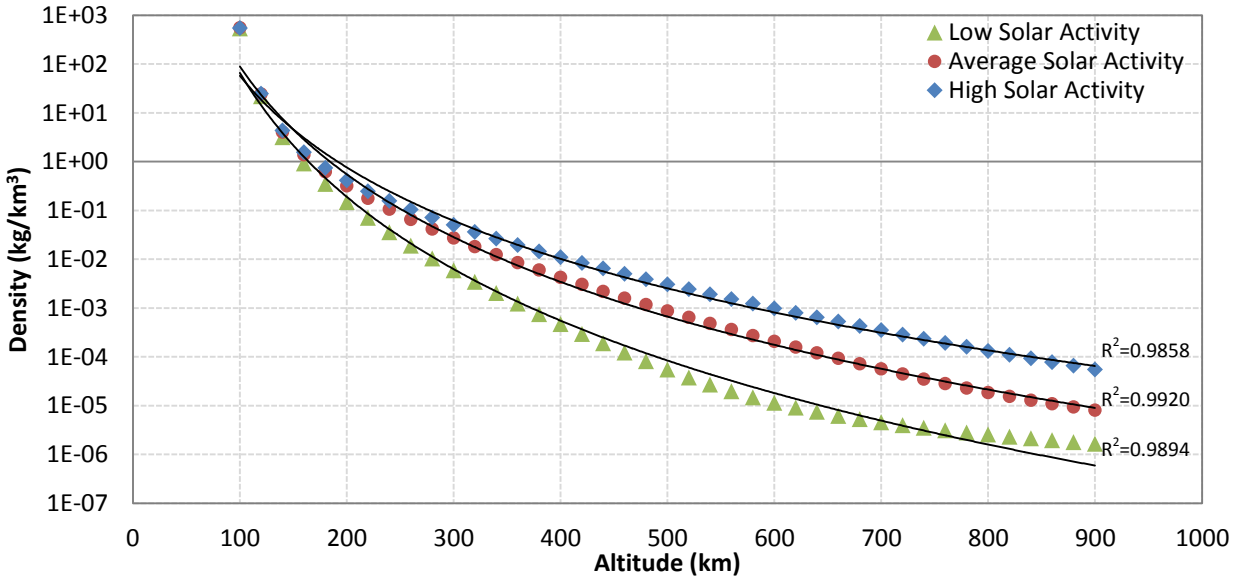

Fig. 2 Power curve-fit for atmospheric density at low, average, and high solar activity levels; with CIRA-12 data also shown by markers (N.B. logarithmic y-axis).

It can be seen visually in Fig. 2 that the density at any solar activity level is not as accurately described for all altitudes by one complete curve as may be desired. Therefore a series of curves is derived by separating the CIRA density data into subsets of 100km altitude ranges to better fit the data. These series are produced for each of the three solar activity level data sets; the results are shown in Fig. 3. The coefficients required to reproduce the curve fits shown in Fig. 3, using Eq. (2), can be found in the appendix to this paper.

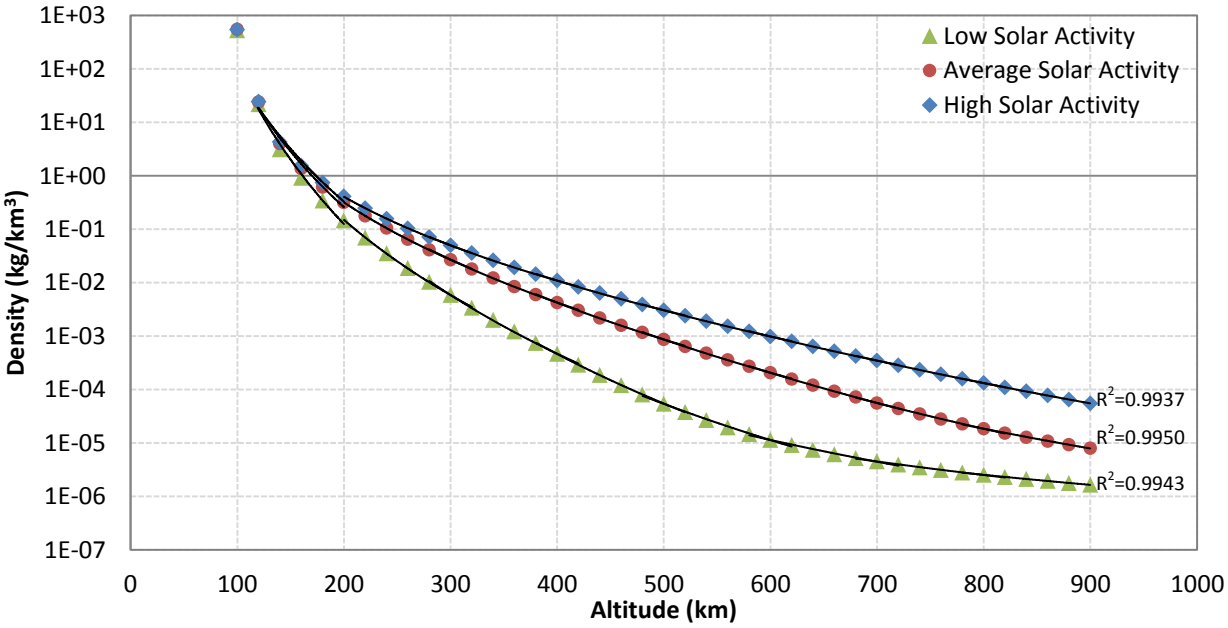

Fig. 3 Segmented power curve-fit for atmospheric density at low, average, and high solar activity levels; with CIRA-12 data also shown by markers (N.B. logarithmic y-axis).

This approach produces a more accurate fit over the entire data set however it can be seen that the transition between curves at lower altitudes is problematic. To solve this problem the curve fits to the 100-200km and 200-300km data subsets are extended to find the point of intersection; for this particular data set and curve fit this is at 180km rather than 200km. This point is then used as the transition altitude to avoid discontinuities in the model. The improvement in accuracy provided by moving from single to multiple curves is minor when considering the R^2 values. However, as will be seen, this minor improvement translates directly into an improvement in lifetime predictions.

The Solar Cycle

The solar activity cycle is a 22-year cycle including two polar reversals. Due to the insensitivity of the $F_{10.7}$ index to magnetic polarity, the solar activity cycle can be considered as an 11-year cycle [35,43]. However, the cycle is

only loosely considered 11 years as each cycle is unique; there have been individual cycles recorded as short as 9 years and as long as 14 years [35]. As shown in Table 1 cycles vary between approximately 9.9 and 11.8 years. Note variables $\Phi, \psi, \upsilon, \xi$ *and* t_0 will be discussed in the next section.

Table 1 Solar activity curve fit properties

Cycle No.	Φ	ψ	υ	ξ	t_0 (Date)	t_0 (Months)	Duration (Years)
18	0.003248	43.63	0.71	70	01-01-1944	0	10.4
19	0.005198	40.14	0.71	70	01-06-1954	125	10.2
20	0.001296	52.58	0.71	70	01-08-1964	247	11.8
21	0.002795	44.89	0.71	70	01-05-1976	388	10.3
22	0.004192	41.66	0.71	70	01-08-1986	511	9.9
23	0.001923	48.35	0.71	70	01-07-1996	630	11.8
24	0.001404	45.73	0.71	70	01-06-2009	785	-

The most respected model of the sun, in current literature, is the magneto-hydrodynamic dynamo model, specifically the Babcock-Leighton dynamo as discussed by Schatten and Pesnell [32]. This model provides a reasonable explanation of the mechanism behind the solar activity cycle. However, it does not well-explain the variation in amplitude of individual cycles. This uncertainty in cycle-to-cycle amplitude means that there is an unavoidable challenge in predicting future cycles [32,44].

The irregular nature of solar activity is often represented using the $F_{10.7}$ index. Fluctuations caused by solar storms are inherently unpredictable and can cause short term spikes in the $F_{10.7}$ index and subsequently the atmospheric density. Generally such spikes average out over time, allowing them to be neglected when considering time periods significantly greater than the duration of the spikes. However, depending on the timeframe being considered an uncertainty should be introduced to account for these spikes. Finally, it should be noted that the use of daily or monthly averaged solar activity data, as applied herein, introduces uncertainty to the input data. Such smoothed data does not demonstrate the true maxima and minima, rather said spikes in solar activity due to, say, solar storms, are smoothed, giving lower maxima and higher minima. Consequently, when averaging this average as performed herein, further uncertainty is introduced.

Solar Forecasting

Following consideration of a range of techniques, including the spectral method, or using precursors [30], regression analysis is found to be the only technique with the maturity and easily malleable nature required for

application herein. Methods such as the spectral method are valid over short periods, however historically they are not accurate when projecting further than a few months. While precursors are a promising technique, particularly the SODA precursor developed by Schatten and Pesnell [32], more research is required to verify their accuracy over long time periods.

The McNish-Lincoln method provides the basis for many other regression analysis methods [45]. It predicts the solar activity cycle up to one year in advance using an average solar activity cycle constructed by sampling a thirteen-month smoothed-cycle running mean at twelve month intervals [46]. Curve fitting is an alternative form of regression analysis; essentially, it uses equations describing the shape of the cycle to predict solar activity up to the end of the current cycle. This is most effective for the middle of the cycle. This is also an inherent weakness as it is only effective from year 2 to year 9 of a typical 11-year cycle; beyond this interval, predictions are more estimation than scientific prediction [46]. The use of an imprecise solar forecast is, however, still recommended over not including solar activity effects at all.

The solar activity cycle is often over-simplified and represented by a sine function. However, there is an asymmetry to the cycle that the sine function cannot properly represent; therefore a different form is required. Changes in cycle length (period) and strength (amplitude) mean that data must be sub-divided into individual periods to accurately describe each cycle. Furthermore, the rising and falling portions of each cycle are often of different durations, as can be seen in close examination of Fig. 4, further complicating the modelling process. The Stewart and Panofsky method was found to fit some cycles relatively well, however some others very poorly [33]. Elling and Schwentek proposed another fit using five independent variables and while it was more successful, it is not ideal for an engineering application, such as that proposed in this paper, due to its complex form and number of variables [34]. However, Hathaway, Wilson, and Reichmann discuss an equation that fits the distribution at least as accurately, while using only 2 independent variables [35]. Their formulation, based on the sunspot number (SSN) data, is

$$SSN(t) = \frac{\alpha(t - t_0)^3}{e^{\frac{(t-t_0)^2}{\gamma^2}} - \kappa}, \tag{3}$$

where t is the time (in months measured relative to a user-selected date), and α, γ, κ, and t_0 whilst constant within each cycle vary from cycle to cycle; α is the amplitude of the cycle, γ is related to the time taken to rise from the initial minimum to maximum, κ provides the asymmetry of the cycle, and t_0 is the starting time (in months measured

relative to a user-selected date) of the particular cycle being considered. Hathaway et al. found that by setting the starting time for a cycle at the solar minimum κ could be fixed to a constant value of 0.71 for all past cycles for which there was sufficient data. With κ fixed, a relationship between γ and α can be developed. This relationship could be attributed to the Waldmeier effect, which states that larger amplitude cycles take less time to reach their maximum than smaller amplitude cycles [47]. There is, however, an argument that this effect is just a statistical fluke that exists in the Wolf sunspot number data rather than a physical property of the solar cycle [48]. For the purposes of this work this relationship is considered to be a true effect that will exist in future cycles.

There is an inherent correlation between sunspot number and solar activity [8]. This correlation means that the Hathaway et al. formulation can be modified to model solar activity. The major difference between the two data sets is the vertical shift, so an independent variable, ξ, is added to the formulation allowing it to be applied to the solar activity distribution rather than sunspot number distribution. The curve fit constants must then be re-derived using the solar activity data. The solar radio flux, SF, (measured in SFU) is then calculated as

$$SF(t) = \frac{\Phi(t - t_0)^3}{e^{\frac{(t-t_0)^2}{\psi^2}} - \upsilon} + \xi \,, \tag{4}$$

where

$$\psi(\Phi) = 22.523 + \frac{33.209}{(\Phi \times 10^3)^{0.385}} \,, \tag{5}$$

and ξ provides the vertical shift. All other parameters are defined the same as in the Hathaway et al. formulation, Φ replacing α, ψ replacing γ and υ replacing κ. Eq. (5) differs from the Hathaway et al. formulation due to the change in the input data set, from sunspot to solar activity data. This new extension of the Hathaway et al. formulation allows a user to bypass the sunspot number and directly calculate the solar activity. It should be noted that, for this and other formulations, the curve fit generated depends on the solar activity data used to generate the curve. Whether the solar activity data is hourly, daily, monthly or yearly averaged will impact the curves parameters; however the formulation itself will remain unchanged. Herein, for ease of processing, monthly averaged solar activity data is used [43].

Solar cycles 18 through 24 are modelled using Eq. (4), see Fig. 4. A prediction for solar activity during the remainder of the current cycle, cycle 24, is also shown in Fig. 4.

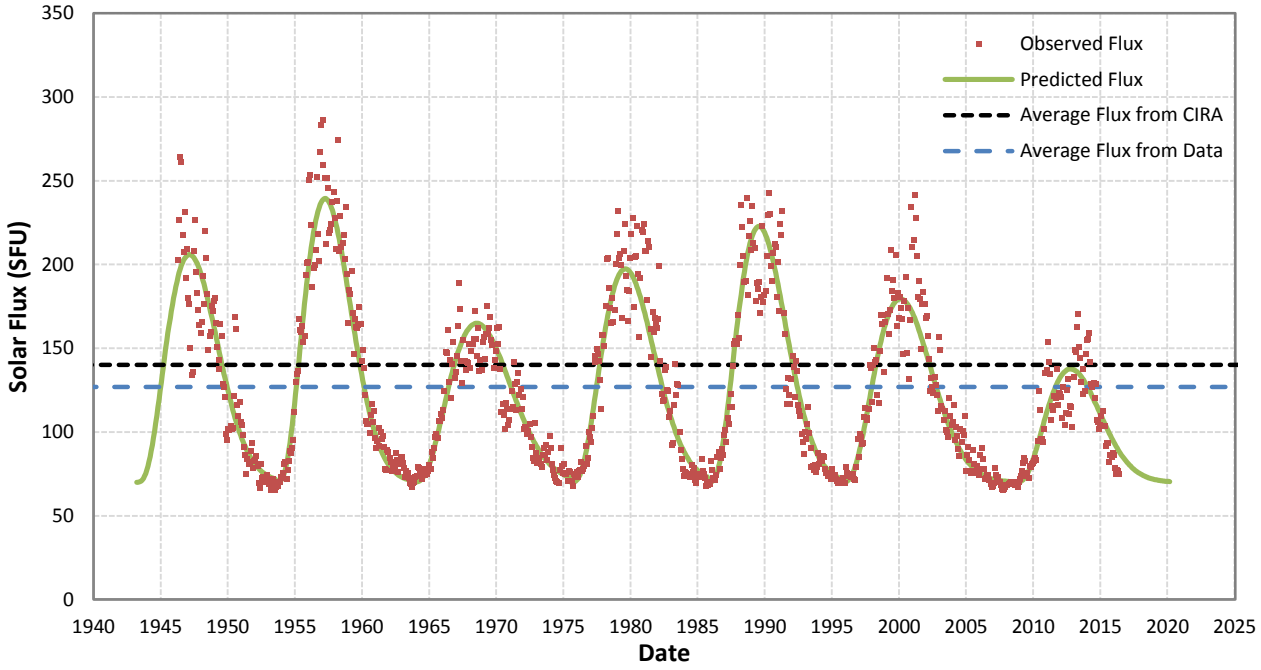

Fig. 4 Solar cycle data.

A series of values for Φ, ψ, υ, ξ and t_0 are determined and used to describe each cycle. Note that in the re-derivation υ and ξ were found to vary slightly from cycle to cycle, however the curve fit was insensitive to these variations so υ and ξ were set at 0.71 and 70 respectively; meaning only one independent variable, Φ, is required. The values used to generate the curve fit shown in Fig. 4 are given in Table 1.

Density Index

The atmospheric density is calculated by introducing a new parameter, the density index, which is a measure of the intensity of solar activity. This parameter is introduced to allow interpolation between the three atmospheric density curves in Fig. 2. The density index is described as

$$DI(t) = \frac{SF - SF_{min}}{SF_{max} - SF_{min}} = \frac{SF - 70}{180}, \tag{6}$$

where DI is the density index, and SF is the solar radio flux. Recall that the values for SF_{min} and SF_{max} are taken as 70 and 250 Solar Flux Units, corresponding respectively to low and high solar activity states as given by the CIRA model. The density index is a dimensionless parameter with a value between 0 and 1, this interval is arbitrary. For the purpose of this work values of 0 and 1 are assigned to a minimum solar activity state and a maximum solar activity states respectively. A value of approximately 0.39 would indicate an average solar activity state due to the

unequal nature of the minimum to average, and average to maximum intervals. The density index effectively allows the extrapolation of an infinite number of solar activity specific curves; meaning atmospheric density calculations are unconfined by minimum, average or maximum states of solar activity, and can instead be discretized by the suitable solar activity specific curve for the problem.

Directly selecting a density index is problematic due to the implicit nature of the problem; the density index required to solve for the orbit lifetime is the average density index calculated over the entire orbit lifetime. For example, if the orbit lifetime is 30 days the density index needed is the average density index over those 30 days. Therefore, an iterative method based on the predicted orbit lifetime is used to converge on the averaged density index and the predicted orbit lifetime.

The atmospheric density is calculated by interpolating between minimum and maximum solar conditions using the density index, giving

$$\rho = \rho_l + DI(\rho_h - \rho_l) \tag{7}$$

where subscripts l, and h indicate low and high solar activity respectively, as defined by the minimum and maximum solar activity states given in the CIRA model.

III. Re-derivation of the King-Hele Model

The solar activity and atmospheric density models developed herein could be applied to any general perturbations or semi-analytical/semi-numerical method. However, for demonstration the King-Hele method is modified to include the new atmospheric model and density index. Before the models are applied, the King-Hele orbit lifetime equations are re-derived using modern mathematical toolsets to remove some of the simplifications made.

Following King-Hele's derivation, the decay of an orbit can be largely characterized by the changes in two of the Keplerian elements: the decrease in the semi-major axis and the decrease in the eccentricity [10]. These can be found directly from Lagrange's Planetary Equations, or from first principles [5]. Lagrange's Planetary Equations can be simplified, for a decaying orbit subject to aerodynamic drag, to

$$\dot{a} = \frac{2a^2 v}{\mu} f_T \tag{8}$$

and

$$\dot{e} = \frac{1}{v}\left[2\, f_T(e + \cos\theta)\right], \tag{9}$$

where v is the velocity of the body in orbit, μ is the standard gravitational parameter of the central body, f_T is the tangential component of drag perturbing the orbit, and θ is the true anomaly.

The most significant perturbation affecting a spacecraft in a low altitude orbit about a body with an atmosphere is atmospheric drag. Therefore the drag force must be calculated, this is done using the standard drag equation [5],

$$D = -\frac{1}{2}\rho v^2 C_D F S, \tag{10}$$

where ρ is atmospheric density at a given altitude, v is the velocity of the body through the atmosphere, C_D is the coefficient of drag of the body, S is the cross-sectional area of the body perpendicular to the direction of travel, and F is a factor taking into account the rotation of the atmosphere, which can be calculated as

$$F = \left(1 - \frac{r\omega}{v}\cos i\right)^2, \tag{11}$$

where r is the orbits radius, ω is the rotational velocity of the atmosphere, and i is the inclination of the orbit. The component of drag in the instantaneous direction of travel, termed the tangential component, f_T is then found by letting

$$\delta = \frac{F\, S\, C_D}{m}, \tag{12}$$

such that

$$f_T = -\frac{1}{2}\rho v^2 \delta. \tag{13}$$

The component of acceleration due to lift is generally considered to be negligible; it is therefore disregarded for the purposes of this work. Substituting Eq. (13) back into and rearranging Eq.'s (8) and (9), they become;

$$\dot{a} = -\frac{\rho\, a^2 v^3 \delta}{\mu} \tag{14}$$

and

$$\dot{e} = -\rho v \delta (e + \cos\theta). \tag{15}$$

It is, however, more convenient to work in terms of eccentric anomaly. The geometry of an elliptical orbit demonstrates the connection between the eccentric anomaly, E and true anomaly, θ which can be used to transform Eq. (15) so that it becomes

$$\dot{e} = -\rho v \delta \left(\frac{a}{r}(1-e^2)\cos E\right). \tag{16}$$

Then, following the King-Hele derivation method [10], performing an integration with respect to eccentric anomaly such that

$$\frac{de}{dE} = \frac{de}{dt}\Big/\frac{dE}{dt}, \tag{17}$$

where dE/dt is calculated as

$$\dot{E} = \frac{1}{r}\left(\frac{\mu}{a}\right)^{\frac{1}{2}}, \tag{18}$$

Eq. (17) becomes

$$\frac{de}{dE} = -\rho a \delta \left(\frac{a}{r}\right)^{\frac{1}{2}} \left(\frac{r v^2}{\mu}\right)^{\frac{1}{2}} (1-e^2)\cos E. \tag{19}$$

Through extensive manipulation this becomes

$$\frac{de}{dE} = -\rho a \delta \left(\frac{1+e\cos E}{1-e\cos E}\right)^{\frac{1}{2}} (1-e^2)\cos E. \tag{20}$$

Through a similar process Eq. (14) may be manipulated and da/dE can be found as

$$\frac{da}{dE} = -\rho a^2 \delta \frac{(1+e\cos E)^{\frac{3}{2}}}{(1-e\cos E)^{\frac{1}{2}}}. \tag{21}$$

Letting $x = ae$, dx/dE is calculated as

$$\frac{dx}{dE} = a\frac{de}{dE} + e\frac{da}{dE}, \tag{22}$$

and substituting Eq.'s (20) and (21) in, Eq. (22) becomes

$$\frac{dx}{dE} = -\rho a^2 \delta \left(\frac{1+e\cos E}{1-e\cos E}\right)^{\frac{1}{2}} (\cos E + e). \tag{23}$$

Equations (21) and (23) are expanded using a power series expansion. The King-Hele method excludes terms of the order e^3 and higher, thus from this point forward is the Modified King-Hele method. This expansion gives

$$\frac{da}{dE} = -\rho_0 e^{(\beta(a_0-a-x_0))} a^2 \delta \left[1 + 2e\cos E + \frac{3}{4}e^2(\cos 2E + 1) + \frac{1}{4}e^3(\cos 3E + 3\cos E)\right] e^{(\beta x \cos E)} \tag{24}$$

and

$$\frac{dx}{dE} = -a^2\rho_0 \mathbb{e}^{(\beta(a_0-a-x_0))}\delta\,[cos\,E + \frac{1}{2}e(cos\,2E+3) + \frac{1}{8}e^2(cos\,3E + 11\,cos\,E) + \frac{1}{16}e^3(cos\,4E + 8\,cos\,2E + 7)]\mathbb{e}^{(\beta x\,cos\,E)}\ , \tag{25}$$

respectively, where β is the inverse of the density scale height [10] and the subscript 0 denotes initial conditions. Simplifying using the integral form of the Modified Bessel function, then integrating Eq.'s (24) and (25) gives

$$\Delta a = -\rho_0 \mathbb{e}^{(\beta(a_0-a-x_0))}a^2\delta(2\pi(I_0[\beta x] + 2eI_1[\beta x] + \frac{3}{4}e^2(I_2[\beta x] + I_0[\beta x]) + \frac{1}{4}e^3(I_3[\beta x] + 3I_1[\beta x]))) \tag{26}$$

and

$$\Delta x = -\rho_0 \mathbb{e}^{(\beta(a_0-a-x_0))}a^2\delta(2\pi(I_1[\beta x] + \frac{1}{2}e(3I_0[\beta x] + I_2[\beta x]) + \frac{1}{8}e^2(11I_1[\beta x] + I_3[\beta x]) + \frac{1}{16}e^3(7I_0[\beta x] + 8I_2[\beta x] + I_4[\beta x]))) \ . \tag{27}$$

After simplifying by letting $z=\beta x$ and,

$$y_n = \frac{I_n[z]}{I_1[z]} \tag{28}$$

and dividing Eq. (26) by Eq. (27), da/dx can be calculated as

$$\frac{da}{dx} = \frac{y_0 + 2e + \frac{3}{4}e^2(y_2 + y_0) + \frac{1}{4}e^3(y_3 + 3)}{1 + \frac{1}{2}e(3y_0 + y_2) + \frac{1}{8}e^2(11 + y_3) + \frac{1}{16}e^3(7y_0 + 8y_2 + y_4)} \tag{29}$$

.

Finally, expanding using a power series Eq. (29) becomes

$$\frac{da}{dx} = y_0 + \frac{1}{2}e(4 - 3y_0^2 - y_0y_2) + \frac{1}{8}e^2(-29y_0 + 18y_0^3 - 2y_2 + 12y_0^2y_2 + 2y_0y_2^2 - y_0y_3) + \frac{1}{16}e^3(-32 + 113y_0^2 - 54y_0^4 + 38y_0y_2 - 54y_0^3y_2 + 2y_2^2 - 18y_0^2y_2^2 - 2y_0y_2^3 + 6y_0^2y_3 + 2y_0y_2y_3 - y_0y_4)\,. \tag{30}$$

To move ahead it is necessary to split into various cases according to eccentricity to treat each more accurately. The cases considered herein are low eccentricity (e < 0.02) and circular (e = 0). The choice of e < 0.02 for the low eccentricity case follows King-Hele's derivation; this assumption is found to be sound for the limited number of cases considered in the validation section of this paper.

Low Eccentricity; e < 0.02

Using the expression

$$\frac{T}{T_0} = \left(\frac{a}{a_0}\right)^{\frac{3}{2}}, \tag{31}$$

where T is the orbit period, and allowing that for one revolution

$$\Delta t = T_0 \left(\frac{a}{a_0}\right)^{\frac{3}{2}}, \tag{32}$$

where t is the orbit lifetime, dividing Eq. (27) by Eq. (32) and expanding further, dx/dt is calculated as

$$\frac{dx}{dt} = \frac{-2\pi\delta {a_0}^2 \rho_0}{T_0} e^{\left[\left(1-\frac{3H}{a_0}\right)Ln\left[\frac{z_0 I_1[z_0]}{z I_1[z]}\right]+\frac{2H}{a_0}\left(z_0\frac{I_0[z_0]}{I_1[z_0]}-z\frac{I_0[z]}{I_1[z]}\right)-\frac{x_0}{H}\right]}\left(1-\frac{H}{a_0}Ln\left[\frac{z_0 I_1[z_0]}{z I_1[z]}\right]\right)^{\frac{1}{2}}\left(I_1[z]+\frac{1}{2}e(3I_0[z]+I_2[z])\right), \tag{33}$$

where H is the density scale height. Replacing z and e, Eq. (33) becomes

$$\frac{dz}{dt} = \frac{1}{H}\left[\frac{-2\pi\delta {a_0}^2 \rho_0}{T_0}\left(1-\frac{H}{a_0}Ln\left[\frac{z_0 I_1[z_0]}{z I_1[z]}\right]\right)^{\frac{1}{2}}\left(\frac{x_0 I_1[z_0]}{Hz I_1[z]}\right) \quad e^{\left[-\frac{3H}{a_0}Ln\left[\frac{z_0 I_1[z_0]}{z I_1[z]}\right]+\frac{2H}{a_0}\left(z_0\frac{I_0[z_0]}{I_1[z_0]}-z\frac{I_0[z]}{I_1[z]}\right)-z_0\right]}\left(I_1[z]+\frac{zH}{2a_0}(3I_0[z]+I_2[z])\right)\right]. \tag{34}$$

To simplify Eq. (34) a term *B'* is introduced as

$$B' = \frac{2\pi}{T_0}\delta\rho_0 x_0 I_1[z_0] e^{[-z_0]}. \tag{35}$$

Using *B'* Eq. (34) then becomes

$$\frac{dz}{dt} = -\frac{{a_0}^2 B'}{H^2 z}\left(1-\frac{H}{a_0}Ln\left[\frac{z_0 I_1[z_0]}{z I_1[z]}\right]\right)^{\frac{1}{2}}\left(1+\frac{zH}{2a_0}(3y_0+y_2)\right) \quad e^{\left[-\frac{3H}{a_0}Ln\left[\frac{z_0 I_1[z_0]}{z I_1[z]}\right]+\frac{2H}{a_0}\left(z_0\frac{I_0[z_0]}{I_1[z_0]}-z\frac{I_0[z]}{I_1[z]}\right)\right]}. \tag{36}$$

Eq. (36) can then be simplified by rearranging, expanding and using the approximations

$$y_2 = y_0 - \frac{2}{z} \tag{37}$$

and

$$z y_0 = 2 + \frac{1}{5}z^2. \tag{38}$$

Eq. (36) therefore becomes

$$-\frac{{a_0}^2 B'}{H^2}\frac{dt}{dz} = z + \frac{7Hz}{2a_0}Ln\left[z_0 I_1[z_0]\right] - \frac{2Hz{z_0}^2}{5a_0} - \frac{5Hz}{a_0} - \frac{7H}{2a_0}\left(\frac{d}{dz}\left(\frac{1}{2}z^2 Ln\left[z I_1[z]\right]\right)\right) - \frac{7H}{10a_0}z^3. \tag{39}$$

By integrating and rearranging, Eq. (39) becomes

$$B'\tau = \frac{1}{2}{e_0}^2\left(\left(1-\frac{z^2}{{z_0}^2}\right)\left(1-\frac{H}{a_0}\left(5+\frac{11{z_0}^2}{20}-\frac{7z^2}{20}\right)\right)-\frac{7Hz^2}{4a_0{z_0}^2}Ln\left[\frac{z_0 I_1[z_0]}{zI_1[z]}\right]\right). \quad (40)$$

Finally the lifetime can be found by substituting z=0 into Eq. (40); the equation for lifetime is

$$\boldsymbol{\tau_L = \frac{{e_0}^2}{2B'}\left(1-\frac{H}{a_0}\left(5+\frac{11{z_0}^2}{20}\right)\right).} \quad (41)$$

Circular; e = 0

The case for zero eccentricity is much simpler, as all eccentricity terms can be removed early in the derivation. As e=0, Eq. (26) becomes

$$\Delta a = -2\pi\rho_0 a^2\delta e^{(\beta(a_0-a))}. \quad (42)$$

Dividing Eq. (32) by Eq. (42), dt/da is calculated as

$$\frac{dt}{da} = \frac{T_0\left(\frac{a}{a_0}\right)^{\frac{3}{2}}}{-2\pi\rho_0 a^2\delta e^{(\beta(a_0-a))}}. \quad (43)$$

Integrating, Eq. (43) becomes

$$t_0 - t = \frac{HT_0}{2\pi\rho_0{a_0}^2\delta}\left(e^{(\beta(a-a_0))}-1\right), \quad (44)$$

and finally substituting in Eq. (31) the lifetime for a spacecraft in circular orbit is

$$\boldsymbol{\tau_L = \frac{HT_0}{2\pi\rho_0{a_0}^2\delta}\left[1-e^{\beta a_0\left\{\left(\frac{T_f}{T_0}\right)^{\frac{2}{3}}-1\right\}}\right].} \quad (45)$$

The solution found here is identical to that found by King-Hele [10]. This is because the simplifications made in the low eccentricity case when following the King-Hele derivation method were to ignore higher order eccentricity terms, which is not necessary in the zero eccentricity case. Due to the approximations made in the derivation of the low eccentricity method, simply substituting in e = 0 into Eq. (41) does not yield Eq. (45); however the resulting orbit lifetime estimation given by both methods for spacecraft with very low initial eccentricities (e < 0.001) are comparable, as will be seen in the validation section of this paper. In both cases the ρ_0 term can be determined using Eq. (7).

IV. Model Validation Using Historical Data

Validation is conducted using data from historical missions, as detailed in Table 2. With the mass, cross-sectional area, drag coefficient, initial epoch, and orbit of the mission defined from [49–51]. As such, all the parameters affecting the lifetime calculations are fixed and invariable within this validation.

Table 2 Validation mission spacecraft characteristics

Spacecraft Name	NORAD Catalogue No.	Initial Epoch	Mass (kg)	Cross-Sectional Area (m^2)	Drag Coefficient
ODERACS-A	22990	10/02/1994	1.482	0.0081	1.93
ODERACS-B	22991	10/02/1994	1.482	0.0081	1.99
ODERACS-E	22994	11/02/1994	5	0.0182	1.96
ODERACS-F	22995	11/02/1994	5	0.0182	2.01
ODERACS-2A	23471	06/02/1995	5	0.0182	1.97
ODERACS-2B	23472	05/02/1995	1.482	0.0081	1.96
GFZ-1	23558	20/04/1995	20.63	0.0362	2.16
Starshine-1	25769	05/06/1999	39.46	0.181	2.16
Starshine-2	26929	16/12/2001	38.56	0.181	2.15
Starshine-3	26996	30/09/2001	90.04	0.6939	2.01
ANDE-Castor	35694	31/07/2009	50	0.183	2.20‡
ANDE-Pollux	35693	31/07/2009	25	0.183	2.20‡
Calsphere-3	04957	01/01/1983	0.73	0.0507	2.03
Calsphere-4	04958	01/01/1983	0.73	0.0507	2.03
Calsphere-5	04963	06/01/1984	0.73	0.0507	2.03
Cosmos 1427 (Yug-2)	13750	29/12/1982	750	3.141593	2.05
Cosmos 1615 (Yug-3)	15446	20/12/1984	750	3.141593	2.05
Cosmos 2137 (Yug-4)	21190	19/03/1991	750	3.141593	2.05
Cosmos 1450 (T2-1)	13972	06/04/1983	750	3.163622	2.18
Cosmos 1534 (T2-2)	14668	26/01/1984	750	3.163622	2.18
Cosmos 1631 (T2-3)	15584	27/02/1985	750	3.163622	2.18

Attitudes of a decaying spacecraft can be difficult to predict, as most will have lost power by re-entry they are unable to maintain a steady attitude and will tumble, altering the drag coefficient and cross-sectional area, and complicating the analysis. However, each of the satellites in Table 2 was chosen for this validation as they are approximately spherical, removing the uncertainty that would be introduced by the attitude awareness problem.

Atmospheric Density Model: Single Curves vs. Multiple Curves

The Modified King-Hele Method is applied to the spacecraft detailed in Table 2 to test the accuracy of the produced lifetime predictions. Before the method proposed herein is compared to other methods, the single curve

‡ As no drag coefficient is cited in the literature for these missions the ISO standard value of 2.2 was used [3].

and multiple curve models for atmospheric density, as displayed in Fig. 2 and Fig. 3 respectively, are compared. It should be noted that for all predictions made using the new solar activity model, the solar activity data used is only that which would have been available to each mission prior to launch.

Table 3 Lifetime analysis results vs. true lifetimes of validation missions

		Single Density Curves		Multiple Density Curves		
Spacecraft Name	True Lifetime (Days)[51]	Predicted Lifetime (Days)	% Error E_s	Predicted Lifetime (Days)	% Error E_m	$\|E_m\| - \|E_s\|$
ODERACS-A	235.1	240.4	2.2	234.7	-0.2	-2.0
ODERACS-B	235.4	240.0	1.9	233.8	-0.7	-1.2
ODERACS-E	384.4	380.1	-1.1	369.1	-4.0	2.9
ODERACS-F	378.6	374.2	-1.1	363.1	-4.1	2.9
ODERACS-2A	401.4	380.5	-5.2	383.1	-4.6	-0.6
ODERACS-2B	236.1	236.8	0.3	239.4	1.4	1.1
GFZ-1	1523.5	1643.7	7.9	1465.6	-3.8	-4.1
Starshine-1	258.3	314.6	21.8	261.9	1.4	-20.4
Starshine-2	130.7	156.5	19.7	146.0	11.7	-8.1
Starshine-3	477.9	540.0	13.0	447.2	-6.4	-6.6
ANDE-Castor	383.3	343.4	-10.4	359.7	-6.2	-4.2
ANDE-Pollux	240.9	198.7	-17.5	212.6	-11.7	-5.8
Calsphere-3	2479.0	2442.7	-1.5	2419.3	-2.4	0.9
Calsphere-4	2451.7	2419.1	-1.3	2377.5	-3.0	1.7
Calsphere-5	2191.5	2170.2	-1.0	2162.9	-1.3	0.3
Cosmos 1427 (Yug-2)	2469.8	2811.5	13.8	2357.2	-4.6	-9.3
Cosmos 1615 (Yug-3)	1939.2	2368.6	22.1	1969.5	1.6	-20.6
Cosmos 2137 (Yug-4)	1474.3	1848.0	25.3	1464.1	-0.7	-24.6
Cosmos 1450 (T2-1)	2609.2	3122.3	19.7	2543.5	-2.5	-17.1
Cosmos 1534 (T2-2)	2426.3	3001.4	23.7	2423.1	-0.1	-23.6
Cosmos 1631 (T2-3)	2109.1	2682.3	27.2	2104.7	-0.2	-27.0
Average absolute error		11.33 %		3.46 %		
Absolute error standard deviation		9.44 %		3.25 %		

Comparing the average errors, which are calculated by averaging the absolute error from all of the lifetime estimates given in Table 3, it is seen that in using multiple curves to model atmospheric density the method produces errors much smaller than those produced by the same method incorporating the single atmospheric density curves. This can be attributed to the increase in accuracy of the density model; in some cases the single curve density is an order of magnitude different to the multiple curve density, which introduces a huge error in the orbit lifetime calculation.

When considering the multiple curves method it can be seen that with the exception of two missions, the predictions generally fall within the 10% range, in fact the average error is 3.46% and the standard deviation in error is 3.25%. It should be noted that one of the exceptions is the ANDE-Pollux mission which has an undefined drag

coefficient, therefore that result is not necessarily reliable. The other is Starshine-2, which was by far the shortest mission duration considered. Further analysis would be required to confirm, however it can be surmised that due to short-term spikes in solar activity, short period errors are not well-captured within the input monthly averaged solar activity data, and that using weekly or even daily averaged data could reduce the error for this spacecraft. Table 3 is shown in graphical form in Fig. 5.

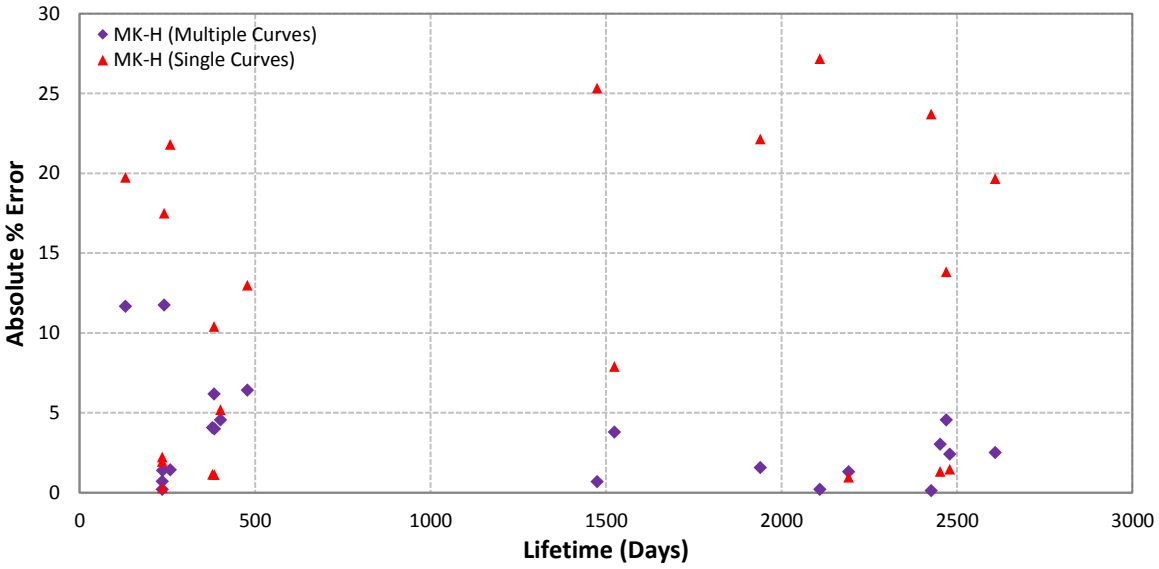

Fig. 5 Method validation for historical spacecraft detailed in Table 2.

When considering the validation results graphically it becomes clear that, while the error in the single curve results mask the trend, the largest errors in the multiple curve method tend to occur in the lowest lifetime missions. This is likely due to a short duration spike in solar activity, which over a longer lifetime is averaged out, but causes a greater uncertainty in the atmospheric density in the short duration. Applying a Monte Carlo analysis with the solar condition input as a variable would address this uncertainty.

If we remove the ANDE spacecraft (the two spacecraft with undefined drag coefficients) from the list the average error from the remaining lifetime estimations decreases to 2.88%. Using this to define upper and lower lifetime boundaries, a range for the drag coefficient of each of these two spacecraft can be derived from the true lifetime: ANDE-Castor likely had a drag coefficient in the range 2.01-2.13, while ANDE-Pollux likely had a coefficient in the range 1.89-2.00.

Lifetime Calculation using Low Eccentricity Equation verses Circular Equation

Equations (41) and (45) are derived based on the eccentricity of the initial orbit; below 0.02 and zero, respectively. The formulation of Eq. (45) is simpler when compared to Eq. (41), which includes a Bessel function, and hence may be preferred for initial analysis. In order to determine the influence of eccentricity on the accuracy of the two lifetime equations the difference in absolute percentage errors in the orbit lifetime estimations given by each equation is examined. This difference is calculated as,

$$Diff = E_C - E_L = \left(\frac{\tau_{L(e=0)} - \tau_{L(true)}}{\tau_{L(true)}} * 100\right) - \left(\frac{\tau_{L(e<0.02)} - \tau_{L(true)}}{\tau_{L(true)}} * 100\right), \quad (46)$$

where E_L and E_C are the absolute percentage errors in Eq. (41) and (45) respectively and τ_L is the orbit lifetime, estimated using Eq. (41) and (45) or the true orbit lifetime from historical record. By considering this difference in the absolute percentage error in the lifetime calculations against the initial orbit eccentricity for the 21 validation missions, see Fig. 6, it is seen that the difference decreases with decreasing eccentricity. Given the structure of Eq. (46), a positive difference in Fig. 6 shows that the low eccentricity equation is more accurate, while a negative difference shows that the circular equation is more accurate. Hence, from the trend shown in Fig. 6, and from the limited data set used, it could be inferred that when the eccentricity drops below approximately 0.001 the orbit may be assumed to be circular, and Eq. (45) could be used without loss of accuracy.

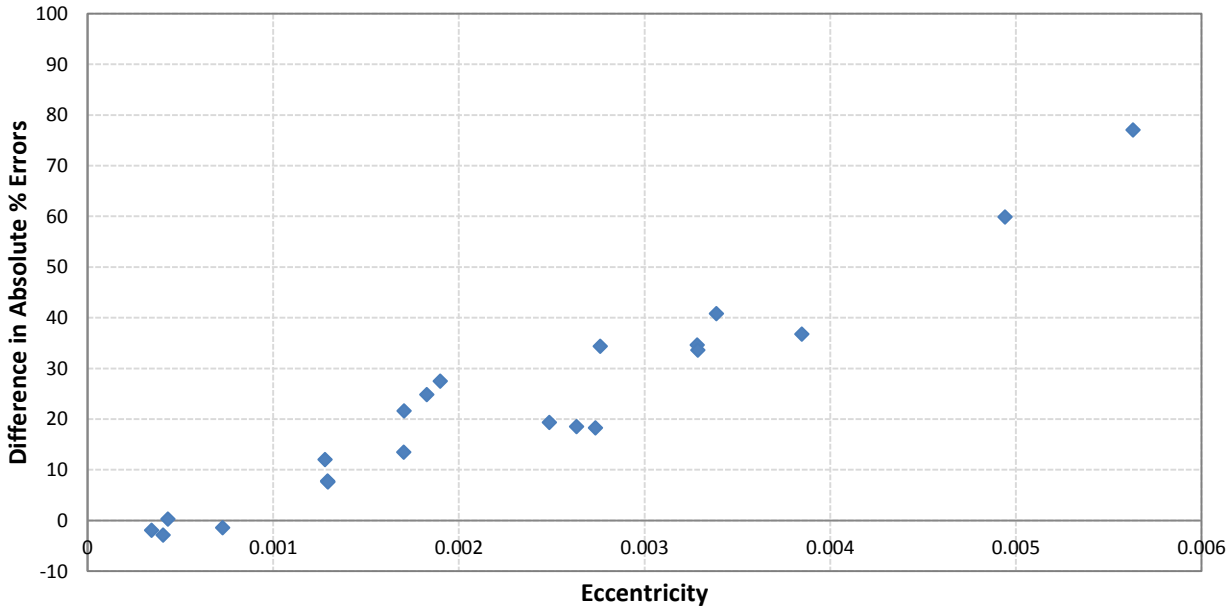

Fig. 6 Comparison of Results using Eq. (41) and Eq. (45)

Comparison to Other Methods

To further verify the proposed method it is tested against other available methods. Two analytical methods are considered: the original King-Hele method, and the Griffin and French method [9,10,12]. Third party software is also considered and while many options for orbit propagation and lifetime estimation exist, currently the most notable are: Systems Tool Kit (STK) from Analytical Graphics, General Mission Analysis Tool (GMAT) from NASA, and Semi-analytical Tool for End of Life Analysis (STELA) from CNES. STK has a Lifetime Analysis Tool that uses a special perturbations algorithm to compute the orbit lifetime of a spacecraft [52]. GMAT was originally designed as a trajectory optimization and mission analysis tool; however, it is capable of performing orbit lifetime analysis. Much like STK, GMAT is a special perturbations tool [53]. STELA was specifically designed to give reliable orbit lifetime estimations, for spacecraft in the LEO and GEO protected regions and in GTO, using a semi-analytical algorithm [54]. It should be noted that neither of the analytical methods directly includes the effects of solar activity; however each of the 3rd party options considered has inbuilt options to include these effects, which were employed in this study.

An orbit lifetime analysis of each of the selected historical missions in Table 2 is completed using each of the analytical and third party software methods. The results tabulated in Table 4 and plotted in Fig. 7, show the comparison of the method developed herein, applied to the Modified King-Hele, to the original King-Hele method updated to include the CIRA density multiple curve model and density index. Comparison is also made to the original King-Hele method updated to include just the CIRA density multiple curve model for average solar conditions (i.e. without the density index). Also included for comparison is the Griffin-French analytical method, which is similar to the original King-Hele method, and uses the CIRA density multiple curve model for average solar conditions to calculate lifetime using a standardized equation, however it's derivation limits its appropriate application to initially circular orbits [12].

Table 4 Comparison of accuracy of discussed methods

Method	Average Absolute % Error	Absolute Error Standard Deviation
Modified King-Hele (CIRA density, with DI)	3.46	3.25
Original King-Hele (CIRA density, with DI)	5.10	3.60
Original King-Hele (CIRA density, average solar conditions, no DI)	50.44	24.96
Griffin-French (CIRA density, average solar conditions, no DI)	50.73	25.88
STK	11.39	10.69
STELA	6.63	7.00
GMAT	149.11	161.18

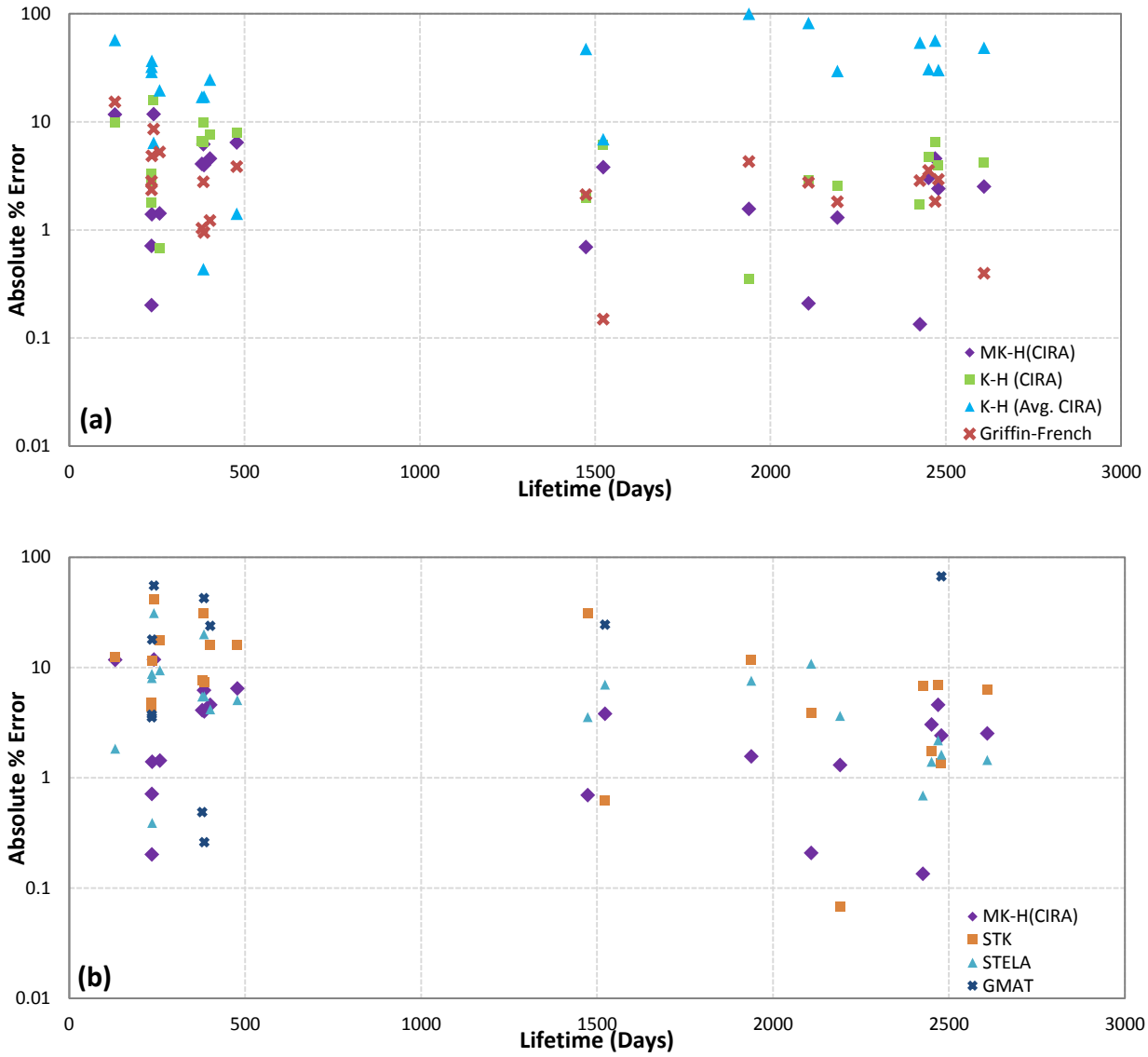

Fig. 7 Accuracy comparison of discussed methods (N.B. logarithmic y-axis); (a) general perturbation methods (b) 3rd party software.

Table 4 shows that the Modified King-Hele method with the new atmospheric model produces the most accurate results. It is the only method that produces an average error of less than 5%; the next best result coming from the original King-Hele method (including new atmospheric and solar activity models) with an average error of 5.1%. This result shows that the modifications made in the re-derivation of the King-Hele method improve accuracy, on average, by approximately 1.5%. However, perhaps of more importance is the comparison of the original King-Hele method with and without the density index included; the inclusion of the density index gives an improvement of around 45%. Thus, it has been shown that the inclusion of solar activity effects on density is vital. The most

accurate third party software is STELA, with an average error of 6.63%. GMAT is found, in this limited trial, to be the least accurate of the compared solutions.

Over the orbit lifetime, perigee, apogee and eccentricity can be plotted to determine exactly how the spacecraft de-orbits. While the projected progression of the decrease in altitude will roughly match between the various methods, the projected progression of the eccentricity will be different. This difference is due to the software giving semi-analytical or numerical solutions, while the Modified and original King-Hele methods are average solutions and thus fail to capture the oscillation in eccentricity.

V. Extending the Modified King-Hele Method with Monte Carlo Analysis

A benefit of general perturbations methods including the Modified King-Hele method is the ability to operate in a so-called batch mode, enabling a user to run multiple simulations, or perform a Monte Carlo analysis without drastically increasing the time taken to solve. The Modified King-Hele method took 8.5 seconds to run a Monte Carlo analysis of 10000 simulations on each of the 21 historical missions detailed in Table 2; amounting to a total of 210000 simulations, each averaging just 40.5 microseconds. This test was done using non-optimized scripts within MATLAB R2014a, on a Windows 7 desktop computer with an Intel i7-3770 operating at 3.4 GHz and 16384 MB of RAM.

Wrapping the Modified King-Hele method in a Monte Carlo analysis offers the chance to see how the variation in parameters such as the initial eccentricity, the spacecraft mass or even the launch date will affect the predicted orbit lifetime. A Monte Carlo analysis can also be used to provide confidence in the predicted lifetime by accounting for uncertainties introduced by including variations in parameters such as solar activity, thereby producing maximum and minimum orbit lifetime bounds for a mission. The probabilities produced by the Monte Carlo analysis can also be fed into higher levels of analysis, such as estimating mission costs, or regulatory compliance checks.

Uncertainties in spacecraft and mission specifications can also be analyzed in the same way to produce estimated orbit lifetime bounds, or a probability distribution can be used to inform the analysis further. Uncertainties in the mass, cross-sectional area, drag coefficient, and launch date cause uncertainty in the lifetime predicted, and a probability distribution can be applied to each variation. Fig. 8 shows the relationship between the variations in each specific parameter to the predicted lifetime of the ODERACS-A spacecraft, while Fig. 9 shows the probability distributions generated by the same variations. These variations are produced using a normal distribution, centered

on the value of each parameter from Table 2, the value for the estimated error in each parameter is selected based on how well defined the parameter is known. In the example case of ODERACS-A the error in mass was set at ±1%, as was the estimated error in cross-sectional area, as these parameters were measured pre-launch and as such are only subject to very small measurement errors. The estimated errors in drag coefficient and density index were ±5% as they are both inferred parameters and as such are more likely to be subject to large errors.

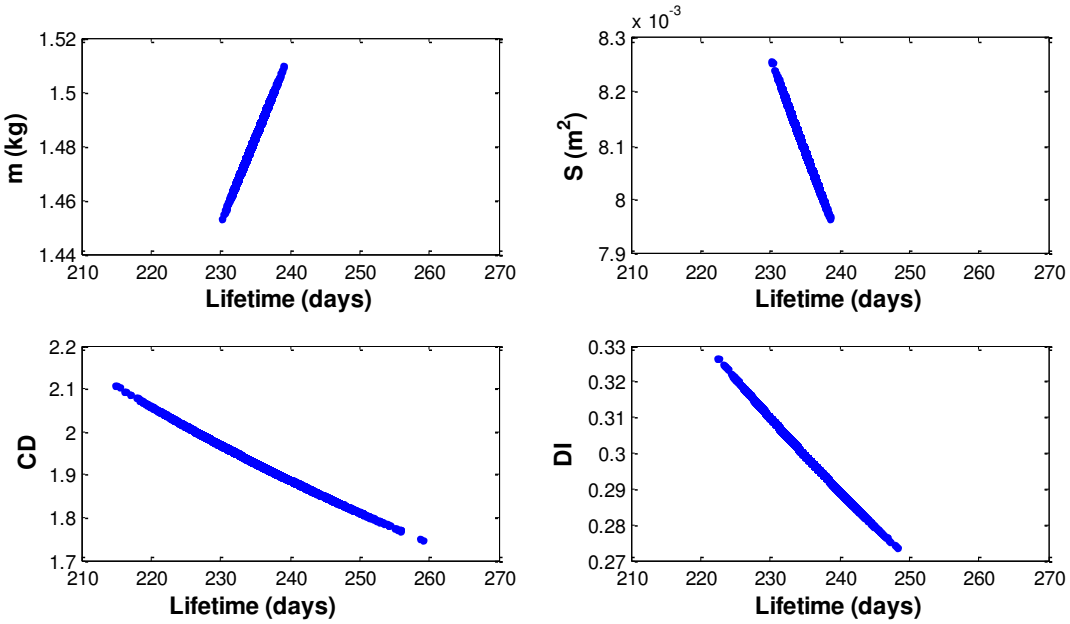

Fig. 8 Monte Carlo analysis of ODERACS-A lifetime – Effects of variations in individual parameters.

It can be seen that while the variation in mass is directly proportional to the orbit lifetime (that is to say, increasing the mass while holding the other parameters constant will increase the orbit lifetime), the cross-sectional area, and drag coefficient are both indirectly proportional. The relationship between the density index and lifetime is more complex; however there is a strong inverse correlation. It is seen here to have a relatively linear relationship; however this is not always the case. These relationships are as expected: increasing the mass, and or decreasing the drag coefficient, and or the cross-sectional area will increase the potential forward momentum of the spacecraft leading to an increased lifetime. Also a decrease in the density index implies a decrease in atmospheric density, which would lead to a longer lifetime.

It should be noted that the launch date is actually a secondary parameter as it informs the density index, which then directly affects the predicted lifetime. These individual variations are overlaid for easy comparison, as seen in Fig. 9.

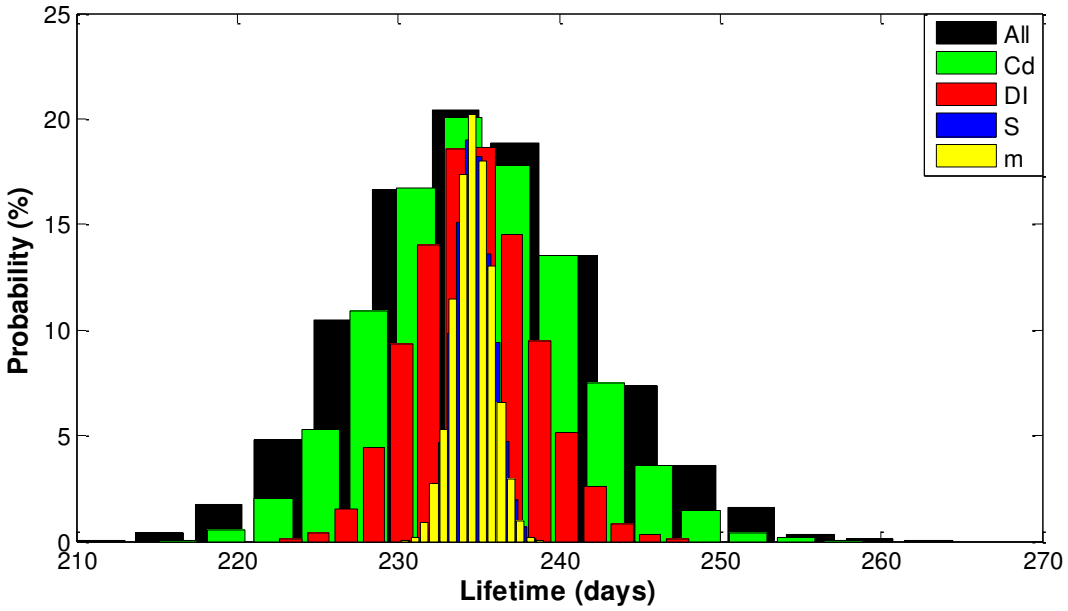

Fig. 9 Monte Carlo analysis of ODERACS-A lifetime – Overlay of individual parameter variations probability distributions.

The overlay shown in Fig. 9 highlights that, for this case, the uncertainty in drag coefficient produced the largest uncertainty in the orbit lifetime predicted, while the uncertainty in the mass produced the smallest uncertainty in predicted orbit lifetime. This can be attributed directly to the percentage error applied due to the directly proportional relationship between variations in mass and lifetime. However upon examination of the spread produced by the density index and drag coefficient, both of which had the same percentage error estimation it becomes clear that variations in the density index has a much smaller effect on the lifetime of this spacecraft due to the complex nature of its relationship to lifetime.

The predicted orbit lifetime of ODERACS-A is around 235 days, as seen in Fig. 9 and Table 3, with a standard deviation of approximately 4 days. This means that the probability of the actual lifetime being in the range 231-239 days is approximately 68% (1σ), whilst the probability of the actual lifetime being in the range 227-243 days is approximately 95% (2σ) and the probability of the actual lifetime being in the range 223-247 days is approximately 99.7% (3σ); the actual lifetime of ODERACS-A was in fact 235 days. By improving the knowledge behind the estimation of parameters, the standard deviation could be decreased and therefore the lifetime ranges produced can be narrowed, or the deviation can be better justified.

Confidence intervals, such as those discussed previously for ODERACS-A, are applied to the entire set of validation missions to further demonstrate the accuracy of the Modified King-Hele method. The 95% (2σ) confidence intervals can be seen in Fig. 10, and the 99.7% (3σ) confidence intervals can be seen in Fig. 11.

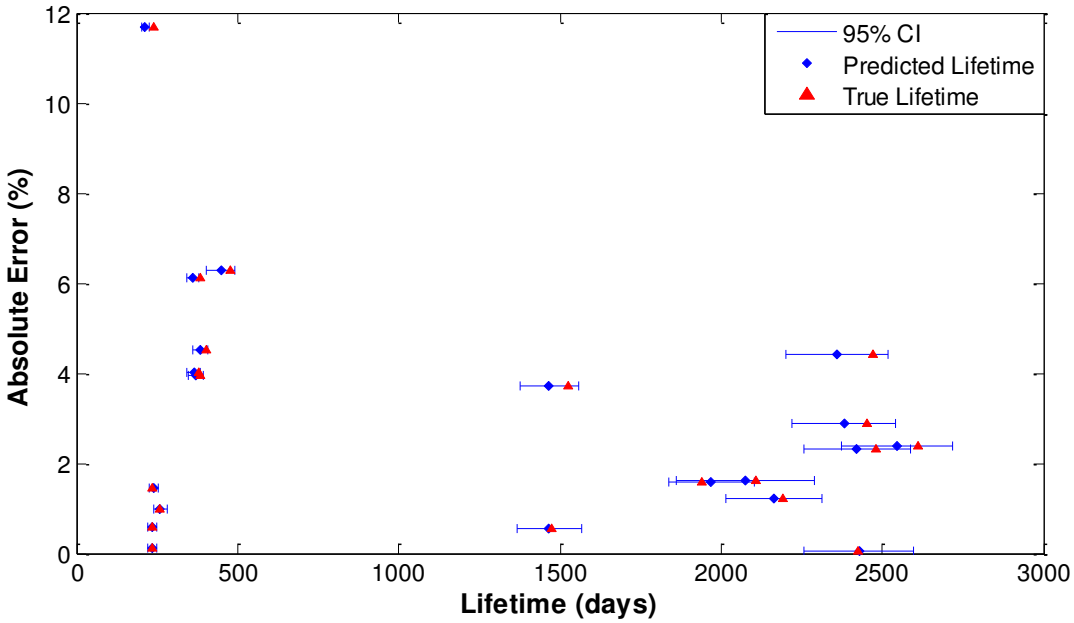

Fig. 10 Monte Carlo analysis of all validation missions with 95% confidence intervals.

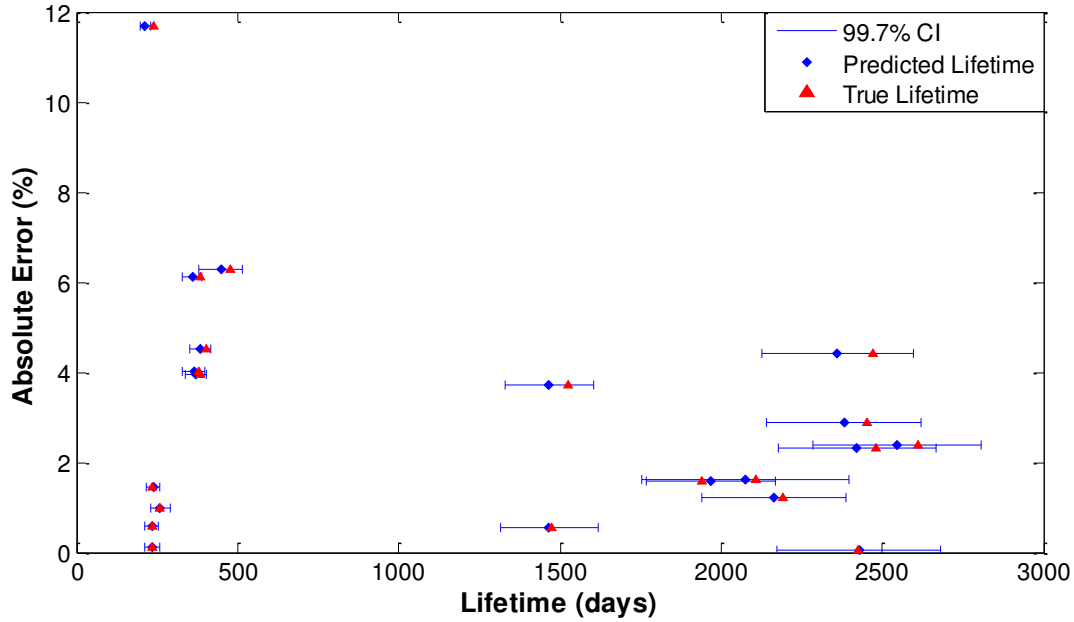

Fig. 11 Monte Carlo analysis of all validation missions with 99.7% confidence intervals.

In Fig. 10 and Fig. 11 the ranges given are the confidence intervals, with diamond markers representing the mean orbit lifetime predictions, whilst the triangle markers show the true orbit lifetime of the spacecraft. It can be seen

that in approximately three-quarters of cases the true lifetime falls within the 95% interval whilst in all but two cases the true lifetime falls within the 99.7% interval. The two cases that exceed the 3σ interval are the same two missions that have errors above 10% (see Table 3), they are both short lifetimes and therefore though they fall outside of the interval the difference between the mean and the true lifetime is within 15 days. Since the confidence intervals are built using percentage variations on the input parameters, it is probable that the shorter the lifetime the more likely that the result will fall outside the confidence interval. And, as previously discussed, short term spikes in solar activity will be more influential in such missions yet are not well-captured in the monthly average data used as input herein.

VI. Case Study – UKube-1

To demonstrate the use of the Modified King-Hele method, with the embedded density index, on a non-historical mission the UKube-1 spacecraft (COSPAR spacecraft identification 2014-037F) is taken as a case study. Unlike the spacecraft used in the validation section, UKube-1 is a standard 3U CubeSat with 3 deployed solar panels. The method derived herein is applied, using the low eccentricity orbit lifetime equation, Eq. (41), to provide an estimate of the maximum altitude that the spacecraft could have been launched to whilst still complying with best practice guidelines (that a spacecraft should deorbit within 25 years of its end of life) [1,2]. Two different predictions for the orbit lifetime of UKube-1 are made. Firstly, conservatively, it is assumed the spacecraft is non-operational from the time it is launched, and hence its orbit must decay within 25 years of orbit insertion. Note that UKube-1 did operate following orbit insertion so this analysis is not a true-to-life prediction, however this analysis would have been applicable pre-launch for regulatory assessment purposes. Secondly, since the spacecraft is now inactive and attitude control actions have ceased [55], it can be assumed that the spacecraft is tumbling randomly. The difference between these predictions will give the benefit to the orbit lifetime from the attitude control.

Pre-launch Orbit Lifetime Analysis

Using UKube-1's actual launch date, specifications and the relevant ISO standard, ISO27852, for drag coefficient and averaged projected area, as defined in Table 5, the maximum allowable altitude can be predicted and a graph of the initial altitude versus the predicted orbital lifetime produced [3]. Note the semi-major axis,

eccentricity, and inclination are taken from orbital tracking data rather than pre-launch estimates, and as such are specified to the level of detail available [51].

Table 5 Parameters used in UKube-1 orbit lifetime analysis

	Launch	Inactive
Date	8th July 2014	9th September 2016
Total mass	3.98 kg	3.98 kg
ISO projected area	0.0628 m^2	0.0628 m^2
Drag coefficient	2.2	2.2
Semi-major axis	7006.23 km	6997.31 km
Eccentricity	0.0003369	0. 0003628
Inclination	98.4032°	98.3371°

The current solar cycle, number 24, is considered a minimum cycle (explicitly its maximum is low when compared to other cycles); however, the magnitude of future cycles cannot be known. Therefore, three possibilities are considered as shown in Fig. 12; that cycles 25 and 26 will both be minimum, average, or maximum cycles. Conservatively, the curve for consecutive minimum cycles should be used to decide a maximum altitude as this will ensure that the spacecraft de-orbits within the 25-year guideline. In the case of UKube-1 it can be seen from Fig. 12 that the maximum allowable altitude would have been approximately 680km, 54km above the actual insertion altitude. UKube-1 is therefore concluded to have been inserted into a lower orbit than necessary to comply with the 25-year limit set out by the ISO and IADC guidelines.

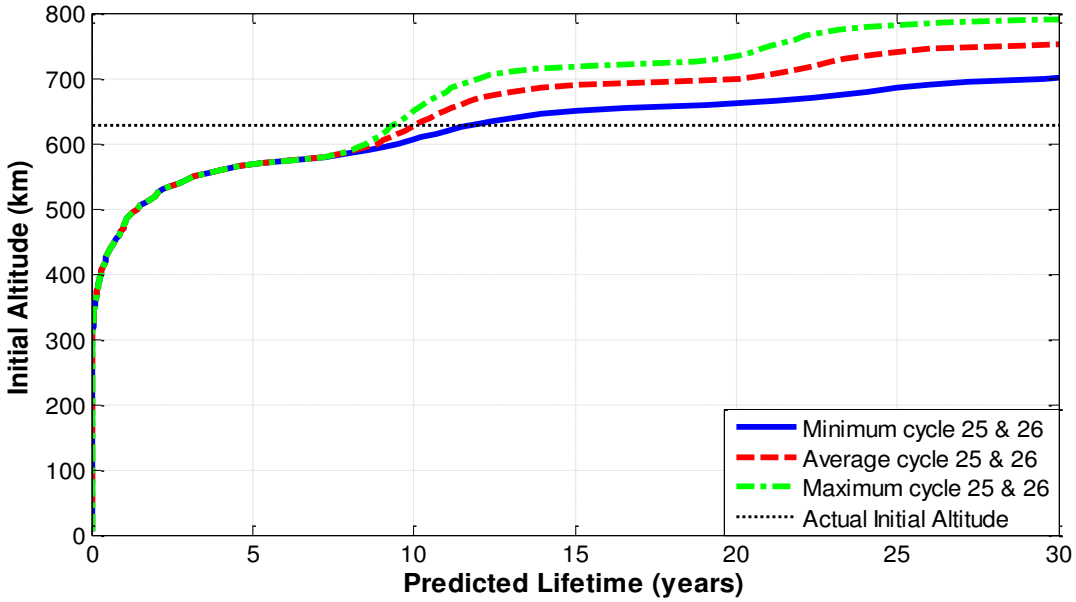

Fig. 12 UKube-1 predicted orbital lifetime versus initial altitude.

If the launch date was still undefined it can be set as a variable in, for example, 1 year steps. Fig. 13 shows the results given three possibilities that the current and future cycles are all minimum, average or maximum cycles. The maximum allowable altitude then becomes a function of the launch date, varying between approximately 670 and 800km depending on the launch date as can be seen in Fig. 13.

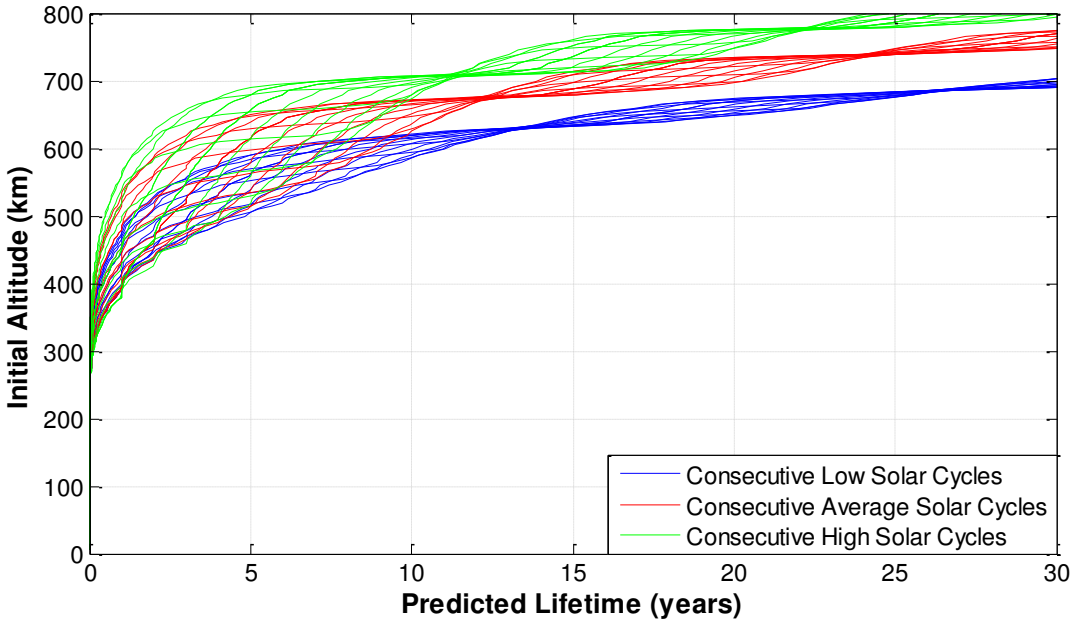

Fig. 13UKube-1 predicted orbital lifetime versus initial altitude with open launch date assuming consecutive low, average and high solar cycles.

It is shown in Fig. 13 that there are points of convergence every 13 years for the group of low cycle curves, and every 12 and 11 years for the average and high cycle groupings, respectively. These points of convergence can be attributed to the cycle period. Thus, when launching to the initial altitudes corresponding to these points of convergence the orbit lifetime predicted will be set regardless of where in the solar cycle the launch occurs. However, the issue with this is that two consecutive solar cycles will never be identical in length and/or strength; this is thus an idealized case.

A maximum allowable altitude prediction is an interesting application of the Modified King-Hele method, and pertinent for documenting compliance with regulatory requirements, however perhaps a more interesting result of the method is the orbit lifetime prediction for UKube-1 given its initial orbit parameters. Given the available data, and the assumptions made herein, it is found that the spacecraft would have deorbited approximately 13.2 years after orbit insertion.

Post Operations Orbit Lifetime Prediction

Once the spacecraft is no longer operational it is assumed that it will begin to tumble randomly. Thus, the ISO standard for average projected area is applied [3]. From Table 5 it is known that during the period of operations UKube-1 decreased approximately 9 km in altitude. From orbit tracking data taken when UKube-1 is known to have been inactive, see Table 5, a further orbit lifetime prediction is made: with 1σ confidence, UKube-1 will de-orbit in approximately 11.8 ± 2 years (June 2026 – June 2030). The confidence bound given on this prediction is generated using a Monte Carlo analysis taking into account uncertainties in the projected area, mass, drag coefficient and solar activity cycle. The largest uncertainty included is the solar activity cycle. As the current cycle will end before UKube-1 decays, the next cycle, which is unknown at present, provides a large uncertainty. The next cycle was considered in the Monte Carlo analysis using a normal distribution fitted around the average solar activity cycle; meaning that it would vary from being a low cycle to a high cycle. However, if the next cycle is simply considered as an average cycle the confidence bounds would contract to 11.8 years ± 4 months (Feb 2028 – October 2028).

When including the 2.2 years of operations this gives a total lifetime for UKube-1 of 13.9 years; meaning the attitude control gave UKube-1 approximately 8 months of extra time in orbit; this is likely the result of UKube-1 maintaining an attitude with a lower projected area than that given by the ISO standard. The average projected decay of UKube-1, from when it is known to be inactive, is shown in Fig. 14.

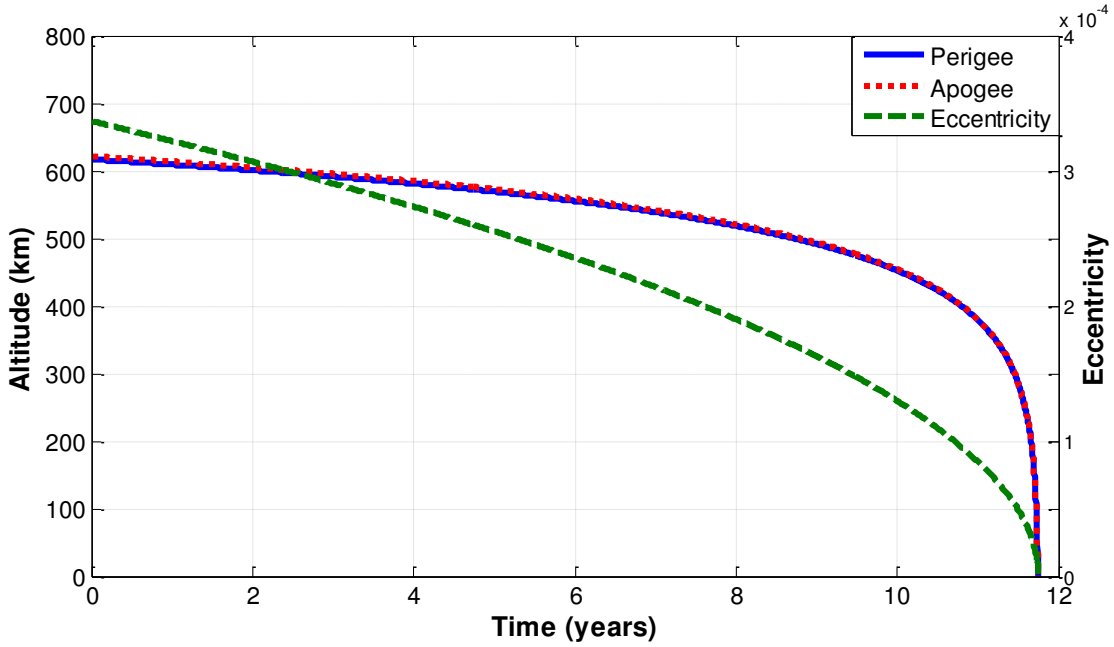

Fig. 14Projected decay of UKube-1.

VII. Conclusion

A single independent variable per solar cycle can be used to relate solar activity levels across a solar cycle. It is thereafter possible to incorporate solar activity into general perturbations solutions using a newly introduced parameter termed the density index. Doing so significantly improves the accuracy of the established solution. Furthermore, it is shown that simplifications, for example removing high-order eccentricity terms, made in the derivation of a well-known method for orbit lifetime prediction can be removed and the accuracy of the analysis improved. The method presented herein compares favorably against other analytical methods and third party tools, producing a significantly lower average error. Notably, the leading software packages examined, STK and STELA, produced predictions with higher average errors of 11.39% and 6.63% respectively, compared to 3.46% with the method presented herein. The improvement in accuracy enables the use of general perturbations methods in areas such as initial mission design and regulatory compliance with confidence.

References

1 International Organization for Standardization, ISO 24113:2011 Space systems - Space debris mitigation requirements, 2011.

2 Inter-Agency Space Debris Coordination Committee, "IADC-02-01 Space Debris Mitigation Guidelines (Revision 1)," 2007, pp. 1–10.

3 International Organization for Standardization, ISO 27852:2010(E): Space systems - Estimation of orbit lifetime, 2010.

4 Oltrogge, D. L., and Chao, C., "Standardized Approaches for Estimating Orbit Lifetime after End-of-Life," AAS/AIAA Astrodynamics Conference, Mackinac Island, MI: 2007, pp. 1–20.

5 Vallado, D. A., and McClain, W. D., Fundamentals of Astrodynamics and Applications, McGraw-Hill Inc., 1997.

6 Macdonald, M., and Badescu, V., eds., The International Handbook of Space Technology, Springer-Verlag Berlin Heidelberg, 2014.

7 Naasz, B. J., Berry, K., and Schatten, K., "Orbit Decay Prediction Sensitivity to Solar Flux Variations," 2007 AIAA/AAS Astrodynamics Specialist Conference, Mackinac Island, MI: 2007.

8 Vallado, D. A., and Finkleman, D., "A critical assessment of satellite drag and atmospheric density modeling," Acta Astronautica, vol. 95, 2014, pp. 141–165.

9 Cook, G. E., King-Hele, D. G., and Walker, D. M. C., "The Contraction of Satellite Orbits under the influence of Air Drag I. With Sphericallly Symmetical Atmosphere," Proceedings of the Royal Society A: Mathematical, Physical and Engineering Sciences, vol. 257, 1960, pp. 224–249.

10 King-Hele, D. G., Satellite Orbits in an Atmosphere: Theory and Application, Glasgow: Blackie and Son Ltd, 1987.

11 Swinerd, G. G., and Boulton, W. J., "Contraction of Satellite Orbits in an Oblate Atmosphere with a Diurnal Density Variation," Proceedings of the Royal Society A: Mathematical, Physical and Engineering Sciences, vol. 383, Sep. 1982, pp. 127–145.

12 Griffin, M. D., and French, J. R., Space Vehicle Design, Reston, VA: American Institute of Aeronautics and Astronautics, Inc., 2004.

13 Sharma, R. K., "Contraction of satellite orbits using KS elements in an oblate diurnally varying atmosphere," Proceedings of the Royal Society A: Mathematical, Physical and Engineering Sciences, vol. 453, Nov. 1997, pp. 2353–2368.

14 Sharma, R. K., "Contraction of high eccentricity satellite orbits using K-S elements with air drag," Proceedings of the Royal Society A: Mathematical, Physical and Engineering Sciences, vol. 454, 1998, pp. 1681–1689.

15 Sharma, R. K., "Analytical approach using KS elements to near-Earth orbit predictions including drag," Proceedings of the Royal Society A: Mathematical, Physical and Engineering Sciences, vol. 433, 1991, pp. 121–130.

16 Sharma, R. K., "A third-order theory for the effect of drag on Earth satellite orbits," Proceedings of the Royal Society A: Mathematical, Physical and Engineering Sciences, vol. 438, 1992, pp. 467–475.

17 Martinusi, V., Dell'Elce, L., and Kerschen, G., "First-order analytic propagation of satellites in the exponential atmosphere of an oblate planet," Celestial Mechanics and Dynamical Astronomy, vol. 127, 2017, pp. 451–476.

18 Martinusi, V., Dell'Elce, L., and Kerschen, G., "Analytic propagation of near-circular satellite orbits in the atmosphere of an oblate planet," Celestial Mechanics and Dynamical Astronomy, vol. 123, 2015, pp. 85–103.

19 Cook, G. E., King-Hele, D. G., and Walker, D. M. C., "The Contraction of Satellite Orbits Under the Influence of Air Drag II. With Oblate Atmosphere," Proceedings of the Royal Society A: Mathematical, Physical and Engineering Sciences, vol. 264, 1961, pp. 88–121.

20 King-Hele, D. G., "The Contraction of Satellite Orbits Under the Influence of Air Drag III. High-Eccentricity Orbits," Proceedings of the Royal Society A: Mathematical, Physical and Engineering Sciences, vol. 267, 1962, pp. 541–557.

21 Cook, G. E., and King-Hele, D. G., "The Contraction of Satellite Orbits Under the Influence of Air Drag IV. With scale height dependant on altitude," Proceedings of the Royal Society A: Mathematical, Physical and Engineering Sciences, vol. 275, 1963, pp. 357–390.

22 Cook, G. E., and King-Hele, D. G., "The Contraction of Satellite Orbits under the Influence of Air Drag V. with Day-To-Night Variation in Air Density," Philosophical Transactions of the Royal Society of London A: Mathematical, Physical and Engineering Sciences, vol. 259, Dec. 1965, pp. 33–67.

23 Cook, G. E., and King-Hele, D. G., "The Contraction of Satellite Orbits Under the Influence of Air Drag VI. Near-Circular Orbits with Day-to-Night Variation in Air Density," Proceedings of the Royal Society A: Mathematical, Physical and Engineering Sciences, vol. 303, 1968, pp. 17–35.

24 King-Hele, D. G., and Walker, D. M. C., "The Contraction of Satellite Orbits under the Influence of Air Drag VII. Orbits of high eccentricity, with scale height dependent on altitude," Proceedings of the Royal Society A: Mathematical, Physical and Engineering Sciences, vol. 411, 1987, pp. 1–17.

25 King-Hele, D. G., and Walker, D. M. C., "The Contraction of Satellite Orbits Under the Influence of Air Drag VIII. Orbital lifetime in an oblate atmosphere, when perigee distance is perturbed by odd zonal harmonics in the geopotential," Proceedings of the Royal Society A: Mathematical, Physical and Engineering Sciences, vol. 414, 1987, pp. 271–295.

26 Barrio, R., and Palacián, J., "High-order averaging of eccentric artificial satellites perturbed by the Earth's potential and air-drag terms," Proceedings of the Royal Society A: Mathematical, Physical and Engineering Sciences, vol. 459, Jun. 2003, pp. 1517–1534.

27 Titov, E., Burt, J., and Josyula, E., "Satellite Drag Uncertainties Associated with Atmospheric Parameter Variations at Low Earth Orbits," Journal of Spacecraft and Rockets, vol. 51, May 2014, pp. 884–892.

28 King-Hele, D. G., and Walker, D. M. C., Technical Report 87030: The Prediction of Satellite Lifetimes,

Farnborough: 1987.

29 Schatten, K., “Solar activity and the solar cycle,” Advances in Space Research, vol. 32, Aug. 2003, pp. 451–460.

30 Schatten, K., “Long-Range Solar Activity Predictions: A Reprieve From Cycle #24’s Activity,” Flight Mechanics Symposium, Greenbelt, MD, USA: NASA Goddard Space Flight Center, 2003.

31 Schatten, K., “Fair space weather for solar cycle 24,” Geophysical Research Letters, vol. 32, 2005.

32 Schatten, K., and Pesnell, W. D., “Solar cycle #24 and The Solar Dynamo,” 20th International Symposium on Space Dynamics, Annapolis, MD, USA: NASA Goddard Space Flight Center, 2007.

33 Stewart, J. Q., and Panofsky, H. A. A., “The Mathematical Characteristics of Sunspot Variations,” The Astrophysical Journal, vol. 88, 1938, pp. 385–407.

34 Elling, W., and Schwentek, H., “Fitting the sunspot cycles 10-21 by a modified f-distribution density function,” Solar Physics, vol. 137, 1992, pp. 155–165.

35 Hathaway, D. H., Wilson, R. M., and Reichmann, E. J., “The Shape of The Sunspot Cycle,” Solar Physics, vol. 151, 1994, pp. 177–190.

36 Commitee on Space Research, COSPAR International Reference Atmosphere - 2012, 2012.

37 Picone, J. M., Hedin, A. E., Drob, D. P., and Aikin, A. C., “NRLMSISE-00 empirical model of the atmosphere: Statistical comparisons and scientific issues,” Journal of Geophysical Research: Space Physics, vol. 107, Dec. 2002, p. SIA 15-1-SIA 15-16.

38 Bowman, B. R., and Tobiska, W. K., “JB2008: The Jacchia-Bowman 2008 Empirical Thermospheric Density Model” Available: http://sol.spacenvironment.net/jb2008/.

39 Bowman, B. R., Tobiska, W. K., Marcos, F. A., Huang, C. Y., Lin, C. S., and Burke, W. J., “A New Empirical Thermospheric Density Model JB2008 Using New Solar and Geomagnetic Indices.”

40 Justus, C. G., and Leslie, F. W., The NASA MSFC Earth Global Reference Atmospheric Model—2007 Version, 2008.

41 Bruinsma, S., Thuillier, G., and Barlier, F., “The DTM-2000 empirical thermosphere model with new data assimilation and constraints at lower boundary: accuracy and properties,” Journal of Atmospheric and Solar-Terrestrial Physics, vol. 65, 2003, pp. 1053–1070.

42 Macdonald, M., McInnes, C., Bewick, C., Visagie, L., Lappas, V., and Erb, S., “Needs Assessment of Gossamer Structures in Communications Platform End-of-Life Disposal,” AIAA Guidance, Navigation and Control

Conference, Boston, Massachusettes, USA: 2013.

43 Space Weather Canada, "Monthly averages of Solar 10.7 cm flux" Available: http://spaceweather.ca/solarflux/sx-5-mavg-en.php.

44 Dikpati, M., and Gilman, P. A., "Simulating and Predicting Solar Cycles Using a Flux Transport Dynamo," The Astrophysical Journal, vol. 649, Sep. 2006, pp. 498–514.

45 Niehuss, K. O., Euler Jr., H. C., and Vaughan, W. W., Statistical Technique for Intermediate and Long-Range Estimation of 13-Month Smoothed Solar Flux and Geomagnetic Index, 1996.

46 Hathaway, D. H., Wilson, R. M., and Reichmann, E. J., "A synthesis of solar cycle prediction techniques," Journal of Geophysical Research, vol. 104, 1999, pp. 22375–22388.

47 Waldmeier, M., "Neue Eigenschaften der Sonnenfleckenkruve," Astronomische Mitteilungen der Eidgenossischen Sternwarte Zurich, vol. 14, 1935, pp. 105–136.

48 Dikpati, M., Gilman, P. A., and De Toma, G., "Tha Waldmeier Effect: An Artifact of the Definition of Wolf Sunspot Number," The Astrophysical Journal, vol. 673, 2008, pp. 99–101.

49 Bowman, B. R., and Moe, K., "Drag Coefficient Variability at 175-500 km from the Orbit Decay Analyses of Spheres," AAS/AIAA Astrodynamics Conference, South Lake Tahoe, California: 2005, pp. 117–136.

50 Qi, Y., Li, H., Xiang, J., and Man, H., "Periodic Variations of Drag Coefficient for the ANDE Spherical Satellites During its Lifetime," Chinese Journal of Space Science, vol. 33, 2013, pp. 525–531.

51 Kelso, T. S., "CelesTrak NORAD Two-Line Element Sets Historical Archives" Available: https://celestrak.com/NORAD/archives/.

52 AGI, "Systems Tool Kit," 2014.

53 NASA, "General Mission Analysis Tool," 2016.

54 CNES, "Semi-analytic Tool for End of Life Analysis," 2016.

55 Walker, H., "Ukube-1: operations and lessons learned," 8th European CubeSat Symposium, London: 2016.

Appendix: CIRA Total Atmospheric Density Curve Fit Coefficients

Table 6 Coefficients required to reproduce the curve fits shown in Fig. 2 using Eq. (2)

	Low Solar Activity $F_{10.7}$=70 SFU		Average Solar Activity $F_{10.7}$=140 SFU		High Solar Activity $F_{10.7}$=230 SFU	
	A	B	A	B	A	B
100-900 km	4.8108354387E+18	-8.4316024345	4.0353801836E+16	-7.3287675685	1.6560406874E+14	-6.2297870621

Table 7 Coefficients required to reproduce the curve fits shown in Fig. 3 using Eq. (2)

	Low Solar Activity $F_{10.7}$=70 SFU		Average Solar Activity $F_{10.7}$=140 SFU		High Solar Activity $F_{10.7}$=230 SFU	
	A	B	A	B	A	B
100-180 km	3.1401475314E+25	-11.5323873660	2.1302781218E+23	-10.4598697530	3.6572435859E+22	-10.0840784840
180-300 km	3.5702302808E+17	-7.9870178011	3.6883393449E+13	-6.1111045267	4.4836934931E+11	-5.2304377430
300-400 km	3.4883419067E+19	-8.7900136027	2.3760454376E+14	-6.4367101996	6.4653842042E+11	-5.2927120099
400-500 km	3.4193579110E+21	-9.5577441366	1.3376579171E+16	-7.1098789385	8.0238678743E+12	-5.7133843080
500-600 km	6.8121896048E+18	-8.5595105119	1.2599509491E+18	-7.8417840857	1.5746908534E+14	-6.1926697178
600-700 km	9.0620295449E+11	-6.0836670624	5.1432928294E+19	-8.4221015808	5.2597040585E+15	-6.7412533040
700-800 km	1.0934691244E+07	-4.3533902868	2.0822606336E+19	-8.2850698109	1.2783834984E+17	-7.2286463032
800-900 km	1.1437831846E+05	-3.6702885332	2.1877054342E+16	-7.2588177982	4.9403188705E+17	-7.4310970797